GALLOPING OF BUNDLE TRANSMISSION LINES

BY

MIN LIAO

A Thesis

Submitted to the Faculty of Graduate Studies

in Partial Fulfillment of the Requirements

for the Degree of

DOCTOR OF PHILOSOPHY

Department of Mechanical and Industrial Engineering

University of Manitoba

Winnipeg, Manitoba.

National Library
of Canada

Acquisitions and
Bibliographic Services

395 Wellington Street
Ottawa ON K1A 0N4
Canada

Bibliothèque nationale
du Canada

Acquisitions et
services bibliographiques

395, rue Wellington
Ottawa ON K1A 0N4
Canada

Your file Votre référence

Our file Notre référence

0-612-23629-3

Canada

THE UNIVERSITY OF MANITOBA

FACULTY OF GRADUATE STUDIES

COPYRIGHT PERMISSION

GALLOPING OF BUNDLE TRANSMISSION LINES

BY

MIN LIAO

A Thesis/Practicum submitted to the Faculty of Graduate Studies of the University of Manitoba in partial fulfillment of the requirements for the degree of

DOCTOR OF PHILOSOPHY

Abstract

A nonlinear model has been developed to investigate the galloping and wake–induced oscillations of an iced twin-bundle transmission line, the low frequency but large amplitude oscillations often observed in the field. Numerical solutions involve a finite element analysis in conjunction with a perturbation scheme to account for a line's geometric nonlinearity, prestress and nonlinear aerodynamic loads. By applying a quasi-steady theory and employing aerodynamic forces obtained from wind tunnel simulations, the initiation of galloping is investigated numerically by using a conventional stability analysis. Limit cycle amplitudes, if oscillations occur, are obtained from an efficient, Krylov-Bogoliubov averaging method and their stability is also studied. In addition, a computationally expedient time marching algorithm is used to compute the response for those instances where averaging procedures cannot be employed. Examples are presented to illustrate typical oscillations of iced, twin conductors.

Acknowledgments

The author would like to express deep gratitude to the thesis advisors Drs. N. Popplewell and A.H. Shah for their academic support and guidance as well as experience and knowledge throughout this work. The helpful discussion with Dr. P. Yu, the computer programs for a single conductor provided by Dr. Y.M. Desai and the aerodynamic data provided by Mr. P. Stumpf are appreciated greatly. The author would also like to acknowledge the assistance and suggestions given by Dr. M.L. Ayari. Sincere appreciation is extended to the author's friend and colleague Dr. P. Zhang for his general help and encouragement.

The financial support provided by Manitoba Hydro, a graduate fellowship from the University of Manitoba and the NSERC research support are gratefully acknowledged.

Table of Contents

List of Tables

List of Figures

Chapter 1

Introduction

1.1 Description and background

Overhead electrical transmission lines consist of single or bundle conductors, insulator strings, support hardware, spacers and tower components (See Figure 1.1 in which the large separation of the two twin bundles excludes their interaction.) Lines are often subjected to wind-induced vibrations of overhead conductors caused by a blast of wind as well as a steady airflow. The conductors' oscillations may lead to flashover as well as wear and fatigue damage to the transmission structure. Eventually, electrical power supply can be severely disrupted.

It has been found economical to use bundle conductors instead of single conductors to transmit electrical power. The commonly used number of conductors per bundle varies from two to four. For twin bundle transmission lines, the two conductors normally lie in a horizontal plane, separated by a distance between 10 and 25 conductor diameters. However, despite the principal advantage of increased capability in power transmission, secondary problems may arise with the bundle conductors. Due to the leeward conductor being immersed in the wake of the windward conductor, the bundles may experience instability caused by a wake vortex. Thus, in addition to the possible aeolian and galloping vibrations observed on single conductors, bundle conductors may be subjected to wake-induced oscillations.

Galloping is characterized by low (0.1 to 3Hz) frequency, large amplitude, self

excited oscillations. It is produced by aerodynamic instabilities that stem from asymmetry in a conductor's cross section due to the ice accretion or, more rarely, the stranding of the conductor cable itself [1]. Galloping instabilities of bundle conductors involve mainly the bulk motion of the bundle. Wake-induced oscillations, on the other hand, are instigated by the aerodynamic forces due to the shielding effects from the windward conductors. They range in frequency from about 0.7 to 6Hz and may involve both a subspan and full span motion when the conductors are connected by spacers. Aeolian vibration is a high frequency and low amplitude oscillation, compared to galloping, that is caused by an alternating wind force arising from a pressure difference due to a regular formation of air vortices behind a conductor.

Modelling the dynamic behavior of a transmission line as well as investigating the effects of aerodynamic forces are challenging tasks because both aspects involve nonlinearities. The object of this research is to study low frequency vibrations, including both galloping and wake-induced oscillations, of twin bundle conductors coated with ice when excited by a steady wind. The ice shapes are obtained from field observations and frozen rain simulations. Aerodynamic forces on the ice coated conductors are measured from static wind tunnel tests. By assuming the conductors' motions to be quasi-static at low frequencies, the measured static aerodynamic forces are applied to dynamic problems after proper modifications.

1.2 Literature review

1.2.1 Introduction

Successful research has been made on a single conductor transmission line that gives fundamental knowledge in understanding the galloping behavior of a transmission

line [1, 2]. However, limited research has been reported for the galloping of bare bundle conductors. Researchers considered the bundle either as an equivalent single conductor [3] or as two rigid cylinders that are either spring mounted or fixed [4, 5, 6, 7]. Little analytical work has been reported for ice coated bundle conductors.

An earlier paper [8] has reviewed the static and dynamic behavior of electrical transmission lines and their mechanical components under wind and ice loading. Recent research on transmission line galloping and wake-induced oscillations has been covered as part of wind excitation [9] and bluff-body, flutter problems [10]. A survey of aeolian vibrations [11] also briefly mentioned the galloping and wake-induced oscillations of both single as well as bundle conductors. The scope of this review highlights analytical studies (that emphasize a transmission line's stability, dynamic behavior and limit cycles) as well as galloping control devices.

1.2.2 Single conductor

Galloping of a transmission line occurs when conductors, which are usually covered with ice or wet snow, are excited by a steady side wind. Its nature has been reviewed by Desai et al [8]. Recently, it has been shown that galloping may also happen on telecommunication cables [12] and cables in a rain [13]. Due to the severe damage that may be caused by galloping, the conditions initiating a conductor's galloping or the resulting limit cycle amplitudes have been studied extensively. Generally, the aerodynamic forces in analytical models are obtained by curve fitting static experimental data and assuming a quasi-static behavior [14, 15]. However, an effort has been made to numerically determine the aerodynamic force coefficients by using a potential flow and boundary integral approach [16]. After employing the equations of motion, the initiation of galloping is determined by assessing the stability at

a conductor's static equilibrium position under wind and ice loading. Galloping vibrations are determined by finding limit cycles [1, 6, 17].

The most commonly used Den Hartog criterion for the vertical galloping of a single conductor (often represented by a single degree of freedom, DOF) considers a conductor's vertical motion only. However, when the conductor's torsional and along-wind motions become important, for certain ice or snow geometries and conductor orientations to the wind, the classical Den Hartog criterion is inadequate and a multiple DOF model is required [13, 18].

Analytical models

The aerodynamic forces acting on a single conductor depend nonlinearly upon the wind speed and relative angle of the wind's attack to the conductor. Such a system is simplified and made numerically tractable by employing a mass–spring–dashpot oscillator consisting of a linear structure and nonlinear, quasi-static forces. The conditions for initiating galloping are obtained by performing an eigenvalue stability analysis on the linearized equations of motion near the conductor's static equilibrium position [18-24]. A three DOF model, which includes the vertical, torsional and along-wind motions, has been developed not only for predicting the galloping instability but also the ensuing nonlinear dynamic motions of a single conductor, the ice shape on which simulates one formed under wet snow [25, 26]. The results from one specific ice shape suggest that the torsional motion, as well as the vertical motion, is significant in initiating a galloping instability [18]. Based upon a two DOF oscillator, which simultaneously considers the vertical and torsional motions, an explicit solution was obtained for the conditions initiating galloping [19, 23]. Furthermore, a geometrical approach has been developed to investigate not only the initiation of galloping but also the critical boundaries where bifurcations happen, as

well as instability trends for conductors having cocentric [20] or eccentric [22] cross-sections. A parametric study gave an understanding of galloping instability and a possible way of alleviating the galloping by changing a system's parameters [20, 22]. However, despite the study of coupled vertical and torsional galloping, the intrinsic coupling between vertical and horizontal movements has not been ignored [24]. It was indicated that vertical galloping may be initiated by a horizontal displacement or velocity.

Both two and three DOF oscillators, as well as two and three dimensional finite element models, have been studied extensively for different internal resonant and non-resonant cases. By using the finite element method, nonlinearities and interactions between various structural modes and different line spans can be accommodated [27]. However, as the number of DOF grows, the computational time increases greatly compared with that for an oscillator – even when a time averaging technique is used.

When the static equilibrium position is unstable, a conductor is prone to gallop and, then, its dynamic behavior should be studied. A prediction of a conductor's steady state limit cycle, which determines the galloping amplitude as well as the frequency and relative phase difference of the vibrating components, has been obtained by using numerical or nonlinear analytical methods [19, 28]. The stability of a limit cycle can be determined by linearly perturbing the limit cycle parameters [1, 23, 29].

A comparison of the results from an oscillator and a finite element analysis has been made by considering the vertical and torsional motions of a conductor. It was found that the limit cycles predicted by a planar finite element idealization are virtually identical to those from a two DOF oscillator representation of a single span line vibrating in one structural mode [19].

The components other than conductors of a transmission line have also been investigated. Most studies of the performance of interphase spacers, spacer–dampers, detuning pendulums and towers have been experimental, as discussed in the later section on galloping control. Cable–stayed structures, including interactions between cables and towers and different restraints and supports, were analyzed to find their static and dynamic equilibrium positions in a steady and quasi–steady wind [30, 31]. It was determined further [32, 33] that a multi–mode galloping of such structures depends upon the initial conditions and the external disturbances.

Numerical and analytical methods

In general, nonlinear differential equations of motion, obtained from either an oscillator or finite element approach, are solved by employing numerical integration or a nonlinear analytical method. The application of a particular solution procedure depends upon the nature of the problem; more than one method can be often applied successfully. The commonly used Krylov-Bogoliubov time averaging method [1, 23, 27], the harmonic balance method [17, 34], the describing function method [28] and multiple scale method [17, 30, 35] can predict steady state solutions of nonlinear equations. Recently, an asymptotic or a perturbation method was applied to a system of weakly coupled, nonlinear wave equations. The equations were formulated by considering the conductor to be a one-dimensional continuum moving vertically [36] as well as in both the vertical and horizontal directions [37]. A trigonometric calculation method has also been developed for the galloping of a single DOF oscillator [38]. When transitions from a quasi-periodicity to chaos occur and the turbulent intermittencies need to be identified, an approximate attractor method can be used [39, 40].

The limit cycle determined by a two DOF (vertical and torsional) oscillator model

was obtained by employing the describing function method [28] as well as the Krylov-Bogoliubov time averaging method [19, 23]. Results obtained from both methods agree with those found from numerical integration [23, 28]. The Krylov-Bogoliubov averaging method has been utilized successfully for different internal resonant and non-resonant cases in conjunction with a three DOF oscillator as well as a three dimensional finite element model [1, 27]. The galloping amplitudes obtained by using the trigonometric calculation method have also been compared with those from the time averaging method. They are essentially identical [38].

1.2.3 Bundle conductors

It has been found economical to transmit electrical power by using two or more bundle transmission conductors, rather than a single conductor. However, bundle conductors may experience both full span and sub-span oscillations because relatively rigid, coupling spacers are introduced between the conductors. Indeed, a leeward conductor can be immersed in the wake of a windward conductor so that the bundle may also experience instability from the aerodynamic forces caused by the wake. Therefore, in addition to possible aeolian and galloping vibrations observed on single conductors, bundle conductors may be subjected to wake-induced oscillations [11, 17].

Wake-induced oscillations

Investigations [4, 5, 6, 7, 41, 42] of the wake effects on bare conductors have been performed by considering two circular cylinders, one in the wake of the other. The aerodynamic forces on the windward conductors are usually assumed to be the same as those on a single conductor. However, the forces created on the leeward

conductors, which are immersed in the wake of the windward conductors, depend nonlinearly upon the conductors' separation [43]. In one set of investigations [4, 7], the windward cylinder was fixed and the leeward cylinder was suspended by a spring and a dashpot. Based on experimental data, the aerodynamic drag and lift coefficients were approximated by polynomial functions of the relative position between the two cylinders. A single DOF model, involving the vertical motion [4], and a two DOF model, accommodating both the horizontal and vertical motions of the leeward cylinder [5, 7, 41] have been employed to find the limit cycle of the leeward cylinder. Again, the limit cycles obtained by the Krylov-Bogoliubov method for wake-induced oscillations agree with those determined from numerical integration [5, 7].

When the windward cylinder is free to move, both cylinders can be modelled by masses supported by springs and dampers [6]. The equations of motion, their solutions and stability can be obtained as before, although higher DOF models are involved. The movement of the windward cylinder significantly affects the motion of the leeward cylinder. For instance, there is a time delay between the motion of the windward cylinder and this motion being "felt" by the leeward cylinder. The time delay is a nonlinear function of not only the positions but also the velocities of both cylinders. Analytical motions incorporating this effect have been found numerically by using Runge-Kutta integration [6, 42].

The wake-induced oscillations and instability of flexible cylinders in an array of fixed cylinders have been investigated for multiple as well as twin conductor bundles. The aerodynamic drag and lift on the flexible cylinders may be found experimentally or analytically. Based on experimental data, both a single DOF idealization [44] of a flexible cylinder and a two DOF representation [45] of two cylinders moving in the cross-flow direction have been evaluated. On the other hand, the aerodynamic drag

and lift, as well as the cylinder's stability, were derived analytically by using a one-dimensional, unsteady integral model [46]. Discrepancies between the experimental and theoretical results were explained by the neglect of vortex shedding, the effect of instabilities caused by fluid fluxes normal to the free air stream and the artificial smoothing of data in the numerical integration.

The combined effects of vortex-induced oscillations and the galloping of a square sectioned cylinder in a cross flow have been investigated by Corless and Parkinson [47]. They suggested that the interactions can be modelled by simply combining the mathematical models of each form taken separately. An improved solution for the primary resonance was developed subsequently based upon the method of multiple scales with a more appropriate asymptotic embedding [48]. The analytical solution was quasi-periodic for weak nonlinearities but, when strong nonlinearities exist, transient chaos was present for certain, physically realizable, parameter values [47].

In addition to an oscillator approach, a finite element analysis has been performed for bundle conductors despite the great computational effort required. Diana et al [49] studied buffeting and galloping by using tensioned beam elements for triple bundles, when full span oscillations are solely of interest at very low, 0.1 to 0.2 Hz frequencies. The equations of motion were solved by employing a Newmark step-by-step, numerical integration. When sub-span motions were also included, an eight or a sixteen DOF cable element, whose lengths equal the sub-span length, has been used to study the vibration of bundle conductors incorporating spacers [50]. Another alternative is to utilize three–node, isoparametric cable elements representing conductors and beam elements representing spacers [51]. If only the bulk or full–span motion needs to be considered, the constrained motion can be idealized by an equivalent single conductor model, which is much more computationally efficient [52]. Linearized equations of motion were derived for both two and three

dimensional models and the conductor's oscillations and stability were determined numerically.

Alleviation of wake-induced oscillations

Extensive field and laboratory studies and theoretical analyses have been conducted to reduce the possibility of initiating galloping and to decrease the amplitudes of galloping by altering conductors' parameters [2, 53, 54] and adding control devices [55-63]. The amplitude, of course, relates directly to the frequency of flashovers between vertically aligned phases and to the severity of mechanical damage to towers and hardware.

Due to the complexity of wake-induced oscillations, an exhaustive analytical study of the effect of parameter changes has not been performed for conductors. Price and Abdallah [6] studied the individual effects of frequency detuning and mechanical damping as a means of alleviating the oscillations. It was indicated that detuning the modes of vibration was effective in a fixed windward conductor analysis. However, it is unlikely that frequency detuning is particularly beneficial for bundle transmission lines in which a multitude of modes may coalesce. They also showed that increasing the mechanical damping is generally the most effective way of enhancing stability. Damping can raise, in some circumstances, the wind's threshold speed necessary to cause instability and it can also reduce the limit cycle amplitude. In contrast, it has been suggested that only high levels of mechanical damping, in excess of that normally achievable in practice, are beneficial for twin bundles [6, 42].

Summary

Much progress has been made in modelling and theoretically analyzing galloping. Theoretical studies, which complement experimental investigations, include the initiation of galloping, finding the limit cycles of galloping and wake-induced oscillations, parametric studies as well as control techniques. Further advances are still needed, however, to develop practical control devices that are invariably effective.

1.3 Present contributions

This thesis focuses mainly on analytically modelling the dynamic behavior of a twin bundle transmission line as well as investigating the effects of aerodynamic forces. A finite element technique coupled with a perturbation scheme, which may reduce computational time, is employed to derive the nonlinear, algebraic equations. Based on the successful research for a single transmission line [1], two analytical models, an equivalent single conductor and a wake–induced oscillation model, are proposed for simulating a twin conductor bundle's motion. The equivalent single conductor model is proposed for a full span motion. By eliminating the sub–span motion between the two conductors, the total DOF is halved and the computational efficiency is improved greatly. When the sub–span motion needs to be investigated, a program for wake–induced oscillations is developed to take into account both full span and sub-span motions. The program is able to handle non-uniform ice geometries and wind loads along the line. Regardless, the initiation of galloping, the limiting amplitude, if galloping happens, as well as the history of a twin-bundle transmission line's motion are investigated.

1.4 Organization of thesis

General mathematical models and methods are described in Chapter 2 for autonomous nonlinear systems, together with a description of computationally efficient, time averaging scheme (the Krylov–Bogoliubov method), a numerical time integration procedure and their application to the galloping problem. An equivalent single conductor model is developed in Chapter 3 to investigate the full span (bulk motion) of a twin conductor bundle. Both physical and fictitious spacers are assumed to restrict relative movements between conductors and spacers. In the case when full span and sub–span motions are considered simultaneously, the model for wake–induced oscillations is given in Chapter 4. Then a sub–span motion is allowed at all the nodal points not defined by physical spacers. Finally, Chapter 5 summarizes the conclusions and discusses future work.

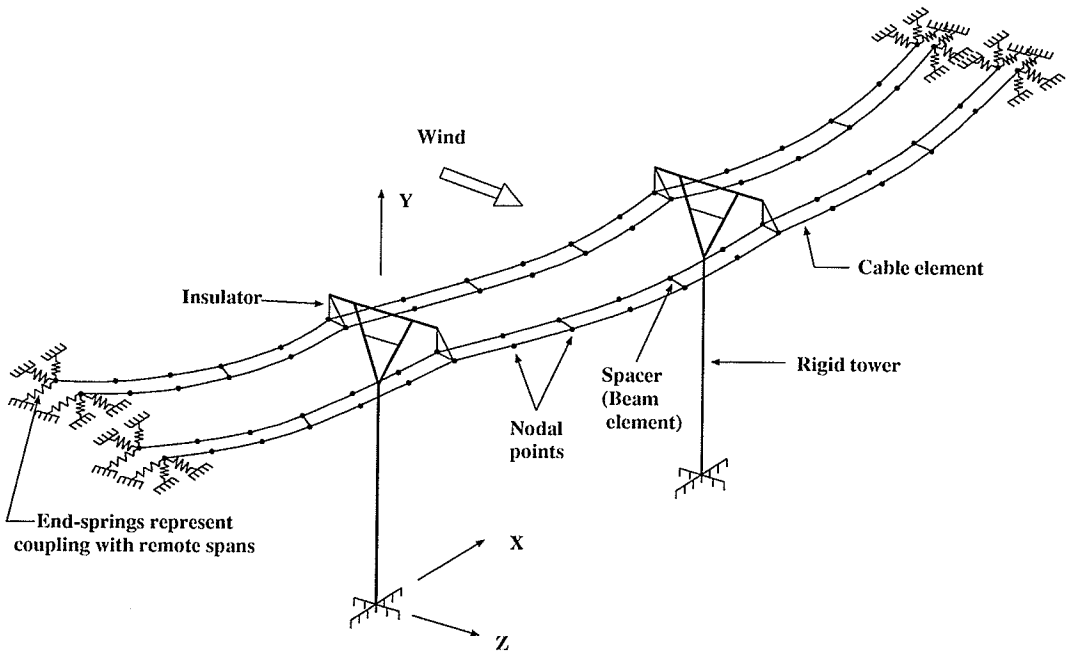

Figure 1.1: Model of a multi–span transmission line

Chapter 2

Mathematical Models and Methods

2.1 Autonomous nonlinear systems

2.1.1 Mathematical models

In the analysis of flow–induced vibrations, mathematical models are generated for both the structure and fluid. Because of their flexibility, cable structures are susceptible to large motions when excited externally. They respond in a geometrically nonlinear fashion to both prestress forces and increasing load, regardless of the material's linearity. The equilibrium configurations, as well as the state of stress, always depend nonlinearly upon the prestress and external static forces. However, the response to dynamic forces may be non-linear or quasi-linear depending on the directions and magnitudes of the dynamic forces relative to the state of stress and configuration of the prestressed structure. In this thesis, cable motions are considered to be near–linear with a varying load near the cable's static equilibrium configuration when the dynamic displacements are assumed small. Therefore, the cable can be simplified to equivalent linear oscillators after the equilibrium configuration has been obtained under a static load.

Fluid models are formed from a combination of quasi–static theory and experimental data. As fluid mechanics is an inherently nonlinear, many degree of freedom phenomenon, it is very difficult to accurately describe the phenomenon by using a general theoretical model. The experimental data needed in modelling the fluid

behavior are obtained from static wind tunnel tests. These data are used in the analysis of a dynamic problem by applying quasi-static theory. In conclusion, a nonlinear autonomous system, which does not explicitly involve time as a variable, is developed to model the cable structure and aerodynamic loads by considering the nonlinearity of both the structure and fluid.

2.1.2 Governing equations of motion

The analysis of oscillations for a weakly nonlinear, autonomous system that has second order differential equations of motion is developed by applying an asymptotic method based on the classical ε order, Krylov-Bogoliubov (KB) method [35, 64, 65, 66]. The general form of N, second order differential equations of motion can be written in principal coordinates as

$$\ddot{\eta}_i + {\omega_i}^2 \eta_i = \varepsilon F_i(\eta_1, \eta_2, \ldots, \eta_{N_p}; \dot{\eta}_1, \dot{\eta}_2, \ldots, \dot{\eta}_{N_p}), \quad i = 1, 2, \ldots, N_p \; ; \; N_p \leq N \; , \tag{2.1}$$

where N_p is the number of principal coordinates, η_i is a generalized displacement, ε is a small parameter ($\varepsilon << 1$), ω_i is a natural frequency of the corresponding linear, undamped system ($\varepsilon = 0$) and εF_i is a modal load containing linear and nonlinear terms. The weak nonlinearity stems from the modal loads, εF_i, which have order ε in comparison to the unit order, inertial and elastic forces.

2.1.3 Solution of the autonomous nonlinear equations

The static equilibrium position of the system described by equation (2.1) corresponds to the zero solution, $\eta = \dot{\eta} = 0$. The first order dynamic solution can be approximated by

$$\eta_i = A_i(t) \cos(\omega_i^* t \; + \; \psi_i(t)) \tag{2.2}$$

where $A_i(t)$ and $\psi_i(t)$ are the unknown, slowly varying ith amplitude and phase, respectively. The ω_i^* are unknown and close to the ith natural frequency, i.e.

$$\omega_i^* = \omega_i + O(\varepsilon). \tag{2.3}$$

The fundamental assumption of the asymptotic analysis is that, for a sufficiently small value of the parameter ε, the solution of equation (2.1) is nearly harmonic but with a slowly varying amplitude and phase over one cycle of oscillation.

Rewrite the periodic solutions of equation (2.1) in the form

$$\eta_i(t) = A_i(t)cos\Psi_i(t), \tag{2.4}$$

$$\Psi_i(t) = \omega_i^* t + \psi_i(t),$$

where $A_i(t)$ and $\Psi_i(t)$ are defined such that

$$\dot{\eta}_i = -A_i\omega_i^* sin\Psi_i, \tag{2.5}$$

$$\dot{A}_i cos\Psi_i = A_i\dot{\Psi} sin\Psi.$$

Then the KB technique is applied to the modified equations

$$\ddot{\eta}_i + \omega^{*2}_i\eta_i = \varepsilon F_i + (\omega^{*2}_i - \omega_i^2)\eta_i, \quad i = 1, 2, \ldots, N_p, \tag{2.6}$$

where $\omega_i^* \equiv \omega_i$, $i = 1, \ldots, k$, for the non-resonant modes and $\omega_i^* = \omega_i + O(\varepsilon)$, $i = 1, \ldots, m$, for the resonant modes. The k and m are the number of the non-resonant and internally resonant modes, respectively, and $k+m = N_p$. Furthermore, the ω_i^* are expressed in terms of a common, but *unknown* frequency ω^* for the resonant modes.

Substituting equations (2.4) and (2.5) into equation (2.6) results in two uncoupled equation sets in $\dot{A}_i$ and $\dot{\psi}_i$, which are given by

$$\dot{A}_i\omega_i^* = [A_i(\omega_i^2 - \omega_i^{*2})cos\Psi_i - \varepsilon F_i]sin\Psi_i, \qquad i = 1, \ldots, N_p, \tag{2.7}$$

and

$$A_i\dot{\psi}_i\omega_i^* = [A_i(\omega_i^2 - \omega_i^{*2})cos\Psi_i - \varepsilon F_i]cos\Psi_i, \qquad i = 1,\ldots,N_p, \tag{2.8}$$

after manipulation. Equations (2.7) and (2.8) are averaged by integrating them with respect to time, t, and by treating slowly varying functions $A_i(t)$ and $\Psi_i(t)$ as constants $\overline{A}_i$ and $\overline{\psi}_i$. The resulting $2N_p$ averaged equations are

$$\dot{\overline{A}}_i\ \omega^* = \frac{1}{T_i}\int_0^{T_i}[A_i(\omega_i^2 - \omega_i^{*2})cos\Psi_i - \varepsilon F_i]sin\Psi_i dt \tag{2.9}$$

$$\overline{A}_i\dot{\overline{\psi}}_i\omega_i^* = \frac{1}{T_i}\int_0^{T_i}[A_i(\omega_i^2 - \omega_i^{*2})cos\Psi_i - \varepsilon F_i]cos\Psi_i dt, \tag{2.10}$$

where T_i is the period of the ith mode. Equations (2.9) and (2.10) now provide an ε order approximation to the system described by equation (2.1).

2.2 Stability analysis

2.2.1 Static configuration and initial stability

In general, a static equilibrium problem is formulated as the solution of [68]

$$P(q) - F = 0, \tag{2.11}$$

where F is a vector of applied loads and P is the nonlinear internal force vector which is indicated to be a function of the nodal parameters q. The residual of the problem, ϕ, is given by

$$\phi(q) = P(q) - F. \tag{2.12}$$

and a solution is defined as any set of nodal displacements, q, for which the residual is zero. The solution is obtained by using the Newton-Raphson (NR) iteration

method, which starts from a state satisfying physical arguments for a solution and then small increments are applied to the loading vector, F. Thus, for any step, a set of values for the components of q is found to satisfy the zero residual condition. By taking small enough steps, a solution path may usually be traced [67].

The initiation of galloping is determined by the stability of the static equilibrium configuration of the transmission line. An unstable static configuration is generally called the initiation phase of galloping. The stability analysis is performed by linearizing the equations of motion near the static equilibrium configuration. The equations of motion generally have the form

$$[M]\{\ddot{q}\} + [C]\{\dot{q}\} + [K]\{q\} = \{F\}, \tag{2.13}$$

where $[M]$, $[C]$ and $[K]$ are the global $N \times N$ structural mass, damping and stiffness matrices, respectively. The cable and beam elements used to model conductors and spacers are described in Appendix A. The $\{F\}$ and $\{q\}$, on the other hand, are the external dynamic force and nodal displacement vectors measured from the equilibrium configuration of the structure. Therefore, the N linearized equations of motion are given by

$$[M]\{\ddot{q}\} + [C_L]\{\dot{q}\} + [K_L]\{q\} = \{0\}, \tag{2.14}$$

where

$$[C_L] \;=\; [C] - [C_U]$$

and

$$[K_L] \;=\; [K] - [K_U] \quad . \tag{2.15}$$

The $[C_U]$ and $[K_U]$ stem from the linearization of the aerodynamic loads. They are formed by assembling the linearized element load vector, $\{{F_L}^e\}$, where

$$\{{F_L}^e\} = [{C_U}^e]\{\dot{q}^e\} + [{K_U}^e]\{q^e\} \quad . \tag{2.16}$$

Elements of $[{C_U}^e]$ and $[{K_U}^e]$ are presented in Appendix B. Eigenvalues of the resulting characteristic matrix, $[S_c]$, are computed from

$$[S_c] = \begin{bmatrix} [0] & [I] \\ -[M]^{-1}[K_L] & -[M]^{-1}[C_L] \end{bmatrix}. \tag{2.17}$$

Here $[0]$ and $[I]$ are the $N * N$ null and identity matrices, respectively. The static configuration is stable if all the eigenvalues of $[S_c]$ have a negative real part.

2.2.2 Limit cycle and its stability

By considering the equations of motion to be weakly nonlinear, time averaging schemes can be used to approximate the periodic solutions. The equations of motion (2.13) are transformed first to the principal coordinate system, η_i, as [1, 27]

$$\ddot{\eta}_i + \omega_i^2 \eta_i = F_{\eta_i} - \sum_{k=1}^{N_p} c^*_{i,k} \dot{\eta}_k, \quad i = 1, 2, \ldots, N_p, \tag{2.18}$$

where

$$F_{\eta_i} = \sum_{j=1}^{n_p} (\phi_{i,4j-2}\ F_{y_j} + \phi_{i,4j-1}\ F_{z_j} + \phi_{i,4j}\ M_{\theta_j}). \tag{2.19}$$

Here n_p and N_p are the number of nodal points and principal coordinates, respectively. The ω_i^2, $\phi_{i,j}$ and $c^*_{i,k}$, on the other hand, are the squared natural frequencies, elements of the eigenfunction matrix $[\phi]$ and damping matrix $[C^*]$ in principal coordinate system, respectively. By applying infinite time integration ($T \to \infty$) in equations (2.9) and (2.10), the resulting $2N_p$ averaged equations for the amplitudes A_i and phases ψ_i become

$$\dot{\overline{A}}_i \omega_* = \lim_{T \to \infty} \frac{1}{T} \int_0^T [A_i(\omega_i^2 - \omega_i^{*2}) cos\Psi_i - F_{\eta_i} - F_{c_i}] sin\Psi_i dt \tag{2.20}$$

$$\overline{A}_i\dot{\overline{\psi}}_i\omega_i^* = \lim_{T\to\infty}\frac{1}{T}\int_0^T [A_i(\omega_i^2 - \omega_i^{*2})cos\Psi_i - F_{\eta_i} - F_{c_i}]cos\Psi_i dt, \tag{2.21}$$

where

$$F_{c_i} = \sum_{k=1}^{N_p} c_{i,k}^*\ A_k\ \omega_k^* sin\Psi_k.$$

The constants $\overline{A}_i$ and $\overline{\psi}_j$ and frequencies ω_i^*, $i = 1, 2, \ldots, N_p$, $j = 1, 2, \ldots, m$, can be found by letting $\dot{\overline{A}}_i(t) = \dot{\overline{\psi}}_j = 0$ in equations (2.20) and (2.21) and solving the resulting nonlinear algebraic equations. Therefore, the approximation of a limit cycle given by equation (2.4) can be determined.

The stability of a limit cycle is determined by performing a stability analysis on the equations

$$\dot{\overline{A}}_i(t) = \sum_{k=1}^{N_p}\frac{\partial\dot{\overline{A}}_i}{\partial A_k}A_k(t) + \sum_{k=1}^{m}\frac{\partial\dot{\overline{A}}_i}{\partial\psi_k}\psi_k(t), \quad i = 1, 2, \ldots, N_p, \tag{2.22}$$

$$\dot{\overline{\psi}}_j(t) = \sum_{k=1}^{N_p}\frac{\partial\dot{\overline{\psi}}_j}{\partial A_k}A_k(t) + \sum_{k=1}^{m}\frac{\partial\dot{\overline{\psi}}_j}{\partial\psi_k}\psi_k(t), \quad j = 1, 2, \ldots, m, \tag{2.23}$$

where m is the number of internally resonant modes. Approximations for the partial derivatives $\partial\dot{\overline{A}}_i/\partial A_j$, $\partial\dot{\overline{A}}_i/\partial\psi_k$, $\partial\dot{\overline{\psi}}_l/\partial A_j$ and $\partial\dot{\overline{\psi}}_l/\partial\psi_k$, $i, j = 1, 2, \ldots, N_p$, $k, l = 1, 2, \ldots, m$, can be obtained from equations (2.9) and (2.10). A $(N_p+m)*(N_p+m)$ characteristic matrix, $[S_c]$, is constructed from equations (2.22) and (2.23) such that

$$\begin{aligned} S_{c_{i,j}} &= \frac{\partial\dot{\overline{A}}_i}{\partial A_j}, \quad S_{c_{i,(N_p+k)}} = \frac{\partial\dot{\overline{A}}_i}{\partial\psi_k}, \\ S_{c_{(N_p+l),j}} &= \frac{\partial\dot{\overline{\psi}}_l}{\partial A_j}, \quad S_{c_{(N_p+l),(N_p+k)}} = \frac{\partial\dot{\overline{\psi}}_l}{\partial\psi_k}, \\ i, j &= 1, 2, \ldots, N_p, \quad k, l = 1, 2, \ldots, m. \end{aligned} \tag{2.24}$$

The signs of the real parts of the eigenvalues of $[S_c]$ determine the stability of the limit cycle. When $m \neq 0$, one eigenvalue is always zero because all the ψ_i are measured with respect to a reference mode. If all other eigenvalues have negative real parts, the limit cycle is stable.

2.3 Numerical time integration

A direct time integration of the equations of motion is performed separately in the principal coordinate system (2.18) as an alternative approach that may be employed to validate the results obtained from the time averaging technique. It may also be performed on the sub-space equations in order to reduce computational effort. The algorithm is summarized below [1].

At time $t = 0$:

The initial $\{\eta\}_0$ and $\{\dot{\eta}\}_0$ are known so that, for the first time step $t = \Delta t$, employ the following formulae

$$\{\eta\}_{\Delta t} = \frac{\Delta t^2}{2}\left[\{F^*\}_0 + \left(\frac{2}{\Delta t^2}[I] - [\Omega]\right)\{\eta\}_0 + \left(\frac{2}{\Delta t}[I] - [C^*]\right)\{\dot{\eta}\}_0\right], \tag{2.25}$$

and

$$\{\dot{\eta}\}_{\Delta t} = \frac{2}{\Delta t}\left(\{\eta\}_{\Delta t} - \{\eta\}_0\right) - \{\dot{\eta}\}_0. \tag{2.26}$$

For the subsequent time steps $t = 2\Delta t, \ldots, t + \Delta t$, use

$$\{\eta\}_{t+\Delta t} = \Delta t^2\left[\{F^*\}_t + \left(\frac{2}{\Delta t^2}[I] - [\Omega]\right)\{\eta\}_t - \frac{1}{\Delta t^2}\{\dot{\eta}\}_{t-\Delta t} - [C^*]\{\dot{\eta}\}_t\right], \tag{2.27}$$

and

$$\{\dot{\eta}\}_{t+\Delta t} = \frac{1}{2\Delta t}\left(3\{\eta\}_{t+\Delta t} - 4\{\eta\}_t + \{\dot{\eta}\}_{t-\Delta t}\right) i, \tag{2.28}$$

where $[\Omega]$ is the diagonal matrix containing the squared natural frequencies and the components of $\{F^*\}$ are defined in equation (2.19).

Chapter 3

Galloping (Bulk Motion) of a Twin Conductor Bundle

3.1 Introduction

It is often observed in the field that twin conductors move in phase with an imperceptible sub-span motion. Therefore, the full span or bulk motion is often studied alone. Then, researchers have considered an equivalent and advantageously simpler single conductor model [1, 2] for a bundle [69]. Moreover, an oscillator analysis based on a damped spring and mass model for twin bundles [3] and a finite element analysis, using tensioned beam elements for triple bundles [49], have been performed. However, further analytical work needs to be performed on the full span oscillations of ice coated as opposed to bare twin-bundle conductors.

In this chapter, the full span bulk motion of an iced twin bundle is investigated, whereas the sub-span motion is neglected. Hence, the twin bundle is modelled as an equivalent single conductor, the motion of which can be represented by the displacements and rotation of a reference curve located midway between the two conductors. A finite element technique is coupled with a perturbation scheme and the nonlinear, algebraic equations are derived and solved. Flexible cable elements are used to represent the conductors and both fictitious and real rigid spacers are assumed to restrict the motion between corresponding nodal points on the two conductors. Compared with the case when both full span and sub-span motions are employed, the resulting computer program is much less time consuming and

needs less storage because the number of variables representing the bulk motion is the same as that for a single conductor. The initiation of galloping, the limiting deflection amplitude if galloping occurs, as well as the history of the twin-bundle transmission line's motion are investigated. Numerical results are given for one iced transmission line and the effects of wind speed as well as the conductors' horizontal tension are studied.

3.2 Formulation

3.2.1 Mathematical model

The bulk motion of a twin bundle is represented by the displacements and rotation of a reference curve between the two conductors. This fictitious curve is designated the center of rotation, as shown in Figure 3.1. It is assumed that the rotation about this center is small and that the longitudinal motions of both conductors are negligible. The conductors are modelled by using computationally efficient, three-node, isoparametric cable elements. Relative movements between two corresponding nodal points on the conductors are constrained by spacers. Rigid spacers link the two conductors at nodal points, e.g., a massless, fictitious spacer joins corresponding conductor nodes not defining a physical spacer. Then, the equivalent single conductor model can take advantage of the results from previous research on single conductors [1].

Equations of motion for two individual conductors

By considering two separate conductors lying side by side, the equations of motion

for the windward and leeward conductors can be written, respectively, as

$$[M_w]\{\ddot{q}_w\} + [C_w]\{\dot{q}_w\} + [K_w]\{q_w\} = \{F_w\} + \{F_{sw}\} \tag{3.1}$$

and

$$[M_l]\{\ddot{q}_l\} + [C_l]\{\dot{q}_l\} + [K_l]\{q_l\} = \{F_l\} + \{F_{sl}\}. \tag{3.2}$$

The $[M_i]$, $[C_i]$ and $[K_i]$, $i = w$ and l, are the $N \times N$ mass, damping and stiffness matrices and subscripts w and l denote the windward and leeward conductors, respectively. Vectors $\{q_w\}$, $\{F_w\}$ and $\{F_{sw}\}$ are the displacements, external aerodynamic loads and the forces simulating the effects of the spacers on the windward conductor, respectively. The $\{q_l\}$, $\{F_l\}$ and $\{F_{sl}\}$ are analogous vectors for the leeward conductor. The effects of the ice formation on the conductors are taken into account when forming the mass and stiffness matrices. The procedure for constructing $[M_w]$ and $[M_l]$, $[C_w]$ and $[C_l]$, as well as $[K_w]$ and $[K_l]$ is similar to that used in reference [1]. Details of these matrices are given in Appendix B for completeness.

Forces on the spacers, $\{F_{sw}\}$ and $\{F_{sl}\}$

Equations of motion for the twin conductor bundle are derived from equations (3.1) and (3.2) in the following section. The forces given by the spacers at each nodal point, j, are denoted as $\{F_{swj}\}$ and $\{F_{slj}\}$ for the windward and leeward conductors, i.e.

$$\{F_{swj}\} \;=\; \{F_{uwj}, F_{vwj}, F_{wwj}, M_{wj}\}, \tag{3.3}$$

and

$$\{F_{slj}\} \;=\; \{F_{ulj}, F_{vlj}, F_{wlj}, M_{lj}\}. \tag{3.4}$$

Here, the F_{uwj}, F_{vwj}, F_{wwj} and M_{wj} are the forces in the x, y and z directions and the (torsional) moment on the windward conductor whilst the F_{ulj}, F_{vlj}, F_{wlj} and M_{lj} are those on the leeward conductor. By using Newton's second law, the relations

between the forces on the spacers and the movements at the center of rotation can be determined. The expressions for the massless fictitious spacers and the physical spacers are

$$\begin{aligned}
-\delta_{sj}\, m_{sj}\, \ddot{u}_j &= F_{ulj} + F_{uwj} \\
-\delta_{sj}\, m_{sj}\, \ddot{v}_j &= F_{vlj} + F_{vwj} \\
-\delta_{sj}\, m_{sj}\, \ddot{w}_j &= F_{wlj} + F_{wwj} \\
-\delta_{sj}\, I_{sj}\, \ddot{\theta}_j &= M_{wj} + F_{vwj}\, l_w\, \cos\theta_{0j} + F_{wwj}\, l_w\, \sin\theta_{0j} \\
&\quad + M_{lj} - F_{vlj}\, l_l\, \cos\theta_{0j} - F_{wlj}\, l_l\, \sin\theta_{0j}\ ,
\end{aligned} \tag{3.5}$$

where

$$\delta_{sj} = \begin{cases} 0 & \text{for a massless, fictitious spacer at node } j \\ 1 & \text{for a physical spacer at node } j\ . \end{cases} \tag{3.6}$$

The I_{sj} and m_{sj} are the inertial moment and mass of the physical spacer at node j. The l_w and l_l are the distances between the center of rotation and the windward and leeward conductors, respectively, for both the real and fictitious spacers. The θ_{0j} is the angle between the spacer and horizontal plane at node j whilst $\ddot{u}_j$, $\ddot{v}_j$, $\ddot{w}_j$ and $\ddot{\theta}_j$ are the accelerations in the x, y and z directions and the angular acceleration of the twin bundle, respectively.

Constrained motions

The movements of both conductors can be expressed in terms of the motion at the center of rotation when the sub–span motion is neglected. Thus, the linear and angular velocities take the matrix form

$$\{\dot{q}_{sj}\} = [T_{sj}]\{\dot{q}_j\}, \qquad s = w \quad \text{and} \quad l, \tag{3.7}$$

for the windward and leeward conductors where $\{\dot{q}_{sj}\}$, $s = w, l$, and $\{\dot{q}_j\}$ are time

derivatives from the displacements and rotations $\{q_{sj}\}$, $s = w, l$, and $\{q_j\}$, respectively. The $\{q_{wj}\} = \{u_{wj}, v_{wj}, w_{wj}, \theta_{wj}\}^T$, $\{q_{lj}\} = \{u_{lj}, v_{lj}, w_{lj}, \theta_{lj}\}^T$ and $\{q_j\} = \{u_j, v_j, w_j, \theta_j\}^T$ represent the displacements in the x, y and z directions and rotations at the windward, leeward conductors and at the center of rotation of the twin bundle at nodal point j, respectively. The transformation matrices $[T_{wj}]$ and $[T_{lj}]$ are defined as

$$[T_{wj}] = \begin{bmatrix} 1 & 0 & 0 & 0 \\ 0 & 1 & 0 & l_w \cos\theta_{0j} \\ 0 & 0 & 1 & l_w \sin\theta_{0j} \\ 0 & 0 & 0 & 1 \end{bmatrix} \quad \text{and} \quad [T_{lj}] = \begin{bmatrix} 1 & 0 & 0 & 0 \\ 0 & 1 & 0 & -l_l \cos\theta_{0j} \\ 0 & 0 & 1 & -l_l \sin\theta_{0j} \\ 0 & 0 & 0 & 1 \end{bmatrix}, \tag{3.8}$$

where θ_{0j} is the initial rotation coordinate at node j at the center of rotation. There are two assumptions made in deriving equations (3.7) and (3.8). The first assumption is that the rotation, θ, is small; the second is that the longitudinal movements of both conductors are identical. Therefore, displacements can be approximated after integration and algebraic manipulation by

$$\{q_{sj}\} \doteq [T_{sj}]\{q_j\}, \qquad s = w \quad \text{and} \quad l. \tag{3.9}$$

Accelerations can be expressed by employing two terms used for the accelerations due to the conductors' tangential and normal components with respect to the center of rotation. The expressions for the accelerations are

$$\{\ddot{q}_{sj}\} = [T_{sj}]\{\ddot{q}_j\} \; + \; [T_{sj0}]\{\dot{q}_j^2\}, \qquad s = w \quad \text{and} \quad l, \tag{3.10}$$

where

$$\{\dot{q}_j^2\} = \{\dot{u}_j^2, \dot{v}_j^2, \dot{w}_j^2, \dot{\theta}_j^2\}^T,$$

$$[T_{wj0}] = \begin{bmatrix} 0 & 0 & 0 & 0 \\ 0 & 0 & 0 & -l_w \sin\theta_{0j} \\ 0 & 0 & 0 & l_w \cos\theta_{0j} \\ 0 & 0 & 0 & 0 \end{bmatrix} \quad \text{and} \quad [T_{lj0}] = \begin{bmatrix} 0 & 0 & 0 & 0 \\ 0 & 0 & 0 & l_l \sin\theta_{0j} \\ 0 & 0 & 0 & -l_l \cos\theta_{0j} \\ 0 & 0 & 0 & 0 \end{bmatrix}. \quad (3.11)$$

Equations of motion for the twin bundle

It can be shown straightforwardly from equations (3.3), (3.4), (3.5) and (3.8), by using Newton's second law, that

$$[T_{wj}]^T\{F_{swj}\} + [T_{lj}]^T\{F_{slj}\} \;=\; -\,\delta_{sj}\,[M_{sj}]\{\ddot{q}_j\} \quad (3.12)$$

for a fictitious as well as a real spacer, where

$$[M_{sj}] = \begin{bmatrix} m_{sj} & 0 & 0 & 0 \\ 0 & m_{sj} & 0 & 0 \\ 0 & 0 & m_{sj} & 0 \\ 0 & 0 & 0 & I_{sj} \end{bmatrix}. \quad (3.13)$$

Finally, by letting

$$\{q_s\} \doteq [T_s]\{q\}, \qquad s = w \quad \text{and} \quad l, \quad (3.14)$$

$$\{\dot{q}_s\} = [T_s]\{\dot{q}\}, \qquad s = w \quad \text{and} \quad l, \quad (3.15)$$

as well as

$$\{\ddot{q}_s\} = [T_s]\{\ddot{q}\} \;+\; [T_{s0}]\{\dot{q}^2\}, \qquad s = w \quad \text{and} \quad l, \quad (3.16)$$

the equations of motion become

$$[M]\{\ddot{q}\} \;+\; [C]\{\dot{q}\} \;+\; [K]\{q\} \;=\; \{F\} \quad (3.17)$$

where $\{q\}$ is the global displacement vector of the bundle at the center of rotation and $\{q_w\}$ and $\{q_l\}$ are the displacement vectors for the windward and leeward conductors, respectively. They are designated

$$\begin{aligned}\{q\}^T &= \{\{q_1\}^T,\ \{q_2\}^T, \ldots,\ \{q_{n_p}\}^T\},\\ \{\dot{q}^2\}^T &= \{\{\dot{q}_1^2\}^T,\ \{\dot{q}_2^2\}^T, \ldots,\ \{\dot{q}_{n_p}^2\}^T\},\end{aligned}$$

where n_p is the number of nodal points at the center of rotation, or the reference curve. The matrices in equation (3.17) are defined as

$$\begin{aligned}[M] &= [T_w]^T[M_w][T_w] + [T_l]^T[M_l][T_l] + [M_s]\\ [C] &= [T_w]^T[C_w][T_w] + [T_l]^T[C_l][T_l]\\ [K] &= [T_w]^T[K_w][T_w] + [T_l]^T[K_l][T_l]\end{aligned} \tag{3.18}$$

and the resultant force vector is given by

$$\{F\} = [T_w]^T\{F_w\} + [T_l]^T\{F_l\}. \tag{3.19}$$

Similarly, the aerodynamic vectors, $\{F_w\}$ and $\{F_l\}$, are assembled from the force vectors $\{F_{wj}\}$ and $\{F_{lj}\}$ whilst the transformation matrices, $[T_w]$ and $[T_l]$, are obtained similarly from matrices $[T_{wj}]$ and $[T_{lj}]$ at nodal point j, $j = 1, \ldots, n_p$. The mass matrix, $[M_s]$, is the contribution from the physical spacers' inertias. More specifically,

$$\{F_s\} = \{\{F_{s1}\}^T, \{F_{s2}\}^T, \ldots, \{F_{sn_p}\}^T\}^T, \qquad s = w \quad \text{and} \quad l, \tag{3.20}$$

$$[T_s] = \begin{bmatrix} T_{s1} & 0 & & \cdots & 0\\ 0 & T_{s2} & 0 & \cdots & 0\\ \vdots & \ddots & \ddots & \ddots & \vdots\\ 0 & \cdots & 0 & T_{s(n_p-1)} & 0\\ 0 & \cdots & & 0 & T_{sn_p}\end{bmatrix}, \qquad s = w \quad \text{and} \quad l, \tag{3.21}$$

and

$$[M_s] = \begin{bmatrix} \delta_{s1}\ M_{s1} & 0 & & \cdots & 0 \\ 0 & \delta_{s2}\ M_{s2} & 0 & \cdots & 0 \\ \vdots & \ddots & \ddots & \ddots & \vdots \\ 0 & \cdots & 0 & \delta_{s(n_p-1)}\ M_{s(n_p-1)} & 0 \\ 0 & \cdots & & 0 & \delta_{sn_p}\ M_{sn_p} \end{bmatrix}. \tag{3.22}$$

The $[T_{w0}]$ and $[T_{l0}]$ are related to the second order velocity terms used in equation (3.16). They have similar definitions to those for $[T_w]$ and $[T_l]$ when T_{wj} and T_{lj} are substituted by T_{wj0} and T_{lj0}, $j = 1, 2, \ldots, n_p$, respectively. However, they are neglected in deriving equation (3.17) because the center of rotation is assumed to be close to the net center of gravity of the two conductors.

3.2.2 Modelling aerodynamic forces

The steady aerodynamic forces, $\{F\}$, in equation (3.17) are obtained directly from experimentally measured static forces and moments at the center of rotation of the twin bundle by applying a quasi–steady theory. These forces, which cause the conductors to vibrate, depend nonlinearly upon the geometry of the iced conductors and the relative wind speed to the conductors. The general form of the aerodynamic forces per unit length can be written, at each nodal point, as

$$\begin{aligned} F_y &= \frac{1}{2}\,\rho_{air}\,U_{rel}^2\,d\,C_y, \\ F_z &= \frac{1}{2}\,\rho_{air}\,U_{rel}^2\,d\,C_z, \end{aligned} \tag{3.23}$$

and

$$M_\theta = \frac{1}{2}\,\rho_{air}\,U_{rel}^2\,d^2\,C_\theta,$$

where ρ_{air}, U_{rel}, d and C_i, $i = y, z, \theta$, are the density of air, relative wind speed with respect to a conductor, a reference structural dimension and the load coefficients, respectively. In this analysis, the coefficients C_y, C_z and C_θ are approximated conventionally by cubic polynomials of the angle of attack at the rotation center, α, to simulate the experimental data. Hence, the polynomials take the general form

$$C_i = \sum_{j=0}^{3} a_{ij}\alpha^j, \qquad i = y, z, \theta, \tag{3.24}$$

where

$$\alpha = \theta - tan^{-1}(\frac{R\dot{\theta} + \dot{v}}{U_z}). \tag{3.25}$$

Here, U_z is the free stream speed in the z direction and R is the characteristic radius corresponding to a reference point where the instantaneous angle of attack is computed [70]. Many researchers simply take $R = 0$ by measuring α at the center of rotation for a single conductor [71, 72, 73, 74]. Others researchers use $R \approx d/2$ by measuring α at a reference point located on the windward side of a single conductor [1, 27]. In this chapter, the constants a_{ij}, $i = y, z, \theta$, $j = 0, 1, 2, 3$, of equation (3.24) are obtained from a least square curve fit of the experimentally measured lift, drag and moment coefficients [1]. These coefficients are calculated as a function of the free stream speed, as well as the relative wind speed for the moving twin conductors, and the instantaneous wind's angle of attack. They are measured along the center of rotation so that R is taken to be zero for solely the bulk motion of the twin bundle conductor.

The rightmost term in the last equation may be approximated by the first linear term in the Taylor series expansion of the inverse tangent function. However, this approximation may give erroneous results, especially when $|R\dot{\theta} + \dot{V}| > 0.6U_z$ for which the error in the computation of α itself is more than 10%. To reduce the error, the next term in the Taylor series is included in the expression for α so that

the approximation

$$\alpha = \overline{\alpha} + \tilde{\alpha}^3/3 \tag{3.26}$$

is used in the time averaging process where

$$\overline{\alpha} = \theta - \tilde{\alpha}$$

and

$$\tilde{\alpha} = (R\dot{\theta} + \dot{v})/U_z. \tag{3.27}$$

3.2.3 Initiation of Galloping

Equations of motion (3.17) define the stability and motion of the conductors' bulk motion. The static configuration of a transmission line, subjected to ice and a mean steady wind load, is computed from the nonlinear, static equilibrium equations obtained by letting $\{\dot{q}\} = \{\ddot{q}\} = 0$ in equation (3.17). The resulting nonlinear static equations,

$$[K]\{q\} = \{F\}, \tag{3.28}$$

are solved by using the NR iteration method described in section 2.2.1 of Chapter 2.

The initiation of galloping is determined by the stability of the static equilibrium configuration of the transmission line. The static configuration is stable if all the eigenvalues of the characteristic matrix, $[S_c]$, determined in equation (2.17) have a negative real part. If the static configuration is unstable, the limiting motion and the history of a motion are found by employing two independent methods, the KB averaging scheme and direct time integration.

3.2.4 Limit cycles

By considering the equations of motion to be weakly nonlinear, time averaging schemes can be used to approximate the periodic solutions. The equations of motion (3.17) are transformed first to the principal coordinate system, η_i, as [1]

$$\ddot{\eta}_i + \omega_i^2 \eta_i = F_{\eta_i} - \sum_{k=1}^{N_p} c^*_{i,k} \dot{\eta}_k, \qquad i = 1, 2, \ldots, N_p, \tag{3.29}$$

where

$$F_{\eta_i} = \sum_{j=1}^{n_p} (\phi_{4j-2,i}\ F_{y_j} + \phi_{4j-1,i}\ F_{z_j} + \phi_{4j,i}\ M_{\theta_j}).$$

Here n_p and N_p are the number of nodal points and principal coordinates, respectively. The ω_i^2, $\phi_{i,j}$, F_{η_i} and $c^*_{i,k}$, on the other hand, are the squared natural frequencies, elements of the eigenfunction matrix $[\phi]$, forcing vector $\{F^*\}$ and the damping matrix $[C^*]$ in the principal coordinate system, respectively. By applying the KB technique to the modified equations

$$\ddot{\eta}_i + \omega^{*2}_i \eta_i = F_{\eta_i} - \sum_{k=1}^{N_p} c^*_{i,k} \dot{\eta}_k + (\omega^{*2}_i - \omega_i^2)\eta_i, \qquad i = 1, 2, \ldots, N_p, \tag{3.30}$$

as described in deriving equation (2.6) of Chapter 2, the resulting $2N_p$ averaged equations (2.9) and (2.10) become

$$\overline{\dot{A}_i \omega_i^*} = \overline{F}_{A_i} = \lim_{T\to\infty} \frac{1}{T} \int_0^T [A_i(\omega_i^2 - \omega_i^{*2}) cos\Psi_i - F_{\eta_i} - F_{c_i}] sin\Psi_i dt \tag{3.31}$$

and

$$\overline{A_i \dot{\psi}_i \omega_i^*} = \overline{F}_{\psi_i} = \lim_{T\to\infty} \frac{1}{T} \int_0^T [A_i(\omega_i^2 - \omega_i^{*2}) cos\Psi_i - F_{\eta_i} - F_{c_i}] cos\Psi_i dt, \tag{3.32}$$

where

$$F_{c_i} = \sum_{k=1}^{N_p} c^*_{i,k}\ A_k\ \omega_k^*\ \sin\Psi_k. \tag{3.33}$$

By substituting equation (3.33) into equations (3.31) and (3.32), the expressions

$$\overline{F}_{A_i} = -\lim_{T\to\infty} \frac{1}{T} \int_0^T \left[\sum_{j=1}^{n_p} F^j_{yz\theta} \right] \sin\Psi_i\ dt - \sum_{k=1}^{N_p} \frac{\delta_{ik}}{2} c^*_{i,k}\ \overline{A}_k\ \omega_k^*\ \cos\overline{\psi}_{ki}, \tag{3.34}$$

and

$$\overline{F}_{\psi_i} = -\lim_{T\to\infty}\frac{1}{T}\int_0^T\left[\sum_{j=1}^{n_p} F^j_{yz\theta}\right]\cos\Psi_i dt - \sum_{k=1}^{N_p}\frac{\delta_{ik}}{2}c^*_{i,k}\,\overline{A}_k\,\omega^*_k\,\sin\overline{\psi}_{ki} + \frac{\overline{A}_i}{2}(\omega_i^2-\omega_i^{*2}) \quad ,i=1,2,\ldots,N_p \tag{3.35}$$

are formed where $F^j_{yz\theta}$, which corresponds to the principal coordinate η_i at nodal point j, is defined as

$$F^j_{yz\theta} = \phi_{4j-2,i}\,F_{y_j} + \phi_{4j-1,i}\,F_{z_j} + \phi_{4j,i}\,M_{\theta_j}\ . \tag{3.36}$$

The phase difference, $\overline{\psi}_{ki}$, and function, δ_{ik}, are given by

$$\overline{\psi}_{ki} = \overline{\psi}_k - \overline{\psi}_i\ , \tag{3.37}$$

and

$$\delta_{ik} = \begin{cases} 1 & \text{if } \omega^*_i = \omega^*_k \\ 0 & \text{if } \omega^*_i \neq \omega^*_k\ . \end{cases} \tag{3.38}$$

After further algebraic modification, equation (3.36) becomes

$$F^j_{yz\theta} = \frac{1}{2}\rho_{air}\,{U_{zj}}^2\,d_j\left(\sum_{k=1}^{3}\overline{a}_k\,\overline{\alpha}^k_j + \delta_\alpha\,\overline{a}_1\,\tilde{\alpha}^3_j/3\ + \delta_\alpha\,\overline{a}_1\,\overline{\alpha}_j\tilde{\alpha}^2_j\right), \tag{3.39}$$

where

$$\overline{a}_p = \phi_{(4j-2),i}\,\overline{a}_{yp} + \phi_{(4j-1),i}\,\overline{a}_{zp} + \phi_{4j,i}\,\overline{a}_{\theta p}\,d_j \quad ,p=1,2,3, \tag{3.40}$$

and

$$\delta_\alpha = \begin{cases} 1 & \text{if } \tilde{\alpha} \text{ is considered to be large} \\ 0 & \text{if } \tilde{\alpha} \text{ is considered to be small}\ . \end{cases} \tag{3.41}$$

The $\tilde{\alpha}$ is considered small when $\tilde{\alpha} << 0.1$ so that the linear approximation reflected in equation (3.26) is reasonable. (This situation is exemplified later in a numerical

example.) The d_j and θ_j are a reference structural dimension and the conductor's rotation at the jth node, whereas $\overline{A}_i$ and $\overline{\psi}_i$ indicate the averaged amplitude and time shift of the ith mode, respectively. The $\overline{a}_{yp}, \overline{a}_{zp}$ and $\overline{a}_{\theta p}$ are computed from

$$\overline{a}_{kp} \;=\; \left(\frac{L_m + L_n}{4}\right)\; a_{kp} \quad ; k = y, z, \theta \;;\; p = 1, 2, 3 \;;\; j = 1, 2, \ldots, n_p \;, \tag{3.42}$$

where L_m and L_n indicate the length of the adjacent mth and nth elements, respectively, to which j ($j \neq 2, 4, 6, \ldots$) is the common node. If $j = 2, 4, 6, \ldots$, then $L_m = L_n = L_e$ is the length of the element for which j is the middle node. The $\overline{\alpha}_j$ and $\tilde{\alpha}_j$ used in equation (3.39) are simplified further to the form

$$\overline{\alpha}_j \;=\; \sum_{n=1}^{N_p} \left(C_n^j \cos\Psi_n \;+\; S_n^j \sin\Psi_n\right) \tag{3.43}$$

and

$$\tilde{\alpha}_j \;=\; -\sum_{n=1}^{N_p} \; S_n^j \sin\Psi_n \tag{3.44}$$

where

$$C_n^j \;=\; \overline{A}_n \; \phi_{4j,n}$$

whilst

$$S_n^j \;=\; \frac{\overline{A}_n \omega_n^*}{U_{zj}} \left(R_j \; \phi_{4j,n} \;+\; \phi_{(4j-2),n}\right) \quad . \tag{3.45}$$

The R_j in the last equation represents the characteristic radius at the jth node and $\phi_{i,j}$ is the ijth element of $[\phi]$. It can be seen from equations (3.34), (3.35), (3.39) and (3.43) that the infinite integration of the products of terms linear, quadratic and cubic in $\overline{\alpha}_j$ as well as linear in θ_j, that are associated with $\sin\Psi_i$ and $\cos\Psi_i$, are required recursively at each jth node, for every ith mode. These integrations have been derived explicitly but are not presented here for brevity. They can be found in [1].

The constants $\overline{A}_i$ and $\overline{\Psi}_j$ and frequencies ω_i^*, $i = 1, 2, \ldots, N_p$, $j = 1, 2, \ldots, m$, are found by letting $\dot{\overline{A}}_i(t) = \dot{\overline{\Psi}}_j = 0$ in equations (3.31) and (3.32) and solving the resulting nonlinear algebraic equations. Therefore the quasi–periodic limit cycle, given by equation (2.4), can be found.

3.2.5 Stability of limit cycles

The stability of a limit cycle is determined by the $(N_p+m)*(N_p+m)$ characteristic matrix, $[S_c]$, constructed from equation (2.24) of Chapter 2. The signs of the real parts of the eigenvalues of $[S_c]$ determine the stability of the limit cycle. When $m \neq 0$, one eigenvalue is always zero because all the ψ_i are measured with respect to a reference mode. If all other eigenvalues have negative real parts, the limit cycle is stable.

3.2.6 Time integration

A direct time integration of the equations of motion is performed separately in the principal coordinate system (3.29) as an alternative approach. The algorithm is summarized by equations (2.25) to (2.28).

3.3 Numerical results

A single span, iced twin conductor bundle is used to illustrate a typical full–span motion when galloping is initiated. The ice accumulations on the conductors, which cause the conductors' instability, are obtained from a simulated freezing rain [1]. The sample designated C11, whose cross–section is illustrated in Figure 3.2(a), resembles

severe icing formed naturally on a single conductor just below 0°C [2]. The icing on the windward and leeward conductors is considered identical in order to use available but limited experimental aerodynamic data. However, about 20% more ice can be accreted in a strong sideways wind on the windward conductor [75]. It is also assumed that each line has a uniform coating of ice and that the wind speed does not change along the span.

The finite element model has 21 nodes at the center of rotation (with node numbers 1 and 21 representing the left and right supports, respectively) so that twenty elements, ten on the windward and ten on the leeward conductor, are used to discretize the two single span conductors. The physical parameters of the conductors are obtained from field measurements and they are listed in Table 3.1. Quasi – static aerodynamic forces are measured in a wind tunnel where the separation between the two rigid C11 models is constant. The separation used here is 0.471 m and, initially, the orientations of models are $\alpha_w = \alpha_l = 40^o$ when the two conductors lie in a horizontal plane, as shown in Figure 3.2(b). These orientations are within the range in which galloping tends to happen [1, 2]. By employing a least square curve fit, the experimental data are found to give the aerodynamic coefficients listed in Table 3.2.

The static profile of the span for the self weight, ice load and static aerodynamic lift and drag forces created by a steady side wind of 4 m/s is shown in Figure 3.3. The horizontal distance between any two adjacent nodal points is always 6.294 m. The horizontal static tension is 30 kN for both simply supported and fixed ends. The only difference between the end conditions is that the longitudinal degree of freedom is retained in the simple support case. However, apart from dead–end spans, a simple support allows a more realistic interaction between adjacent spans so that it is studied in greater detail. The wind speed and tension are chosen so that a 1:1 resonant galloping occurs for both end conditions.

The stability of the static profile of the conductor bundle under the aerodynamic load is investigated to determine the initiation of galloping. The static profile is found to be unstable for both end conditions at the assumed 4 m/s wind speed.

A modal analysis is performed for the $[K]$ and $[M]$ matrices formulated in equation (3.17). The resulting two lowest frequency modes correspond to one loop symmetrical modes for both end conditions, as shown in Figure 3.4. The mode shapes are similar for both cases, the first involves a predominantly horizontal motion and the second is essentially a vertical movement. However, as expected, the second natural frequency is slightly higher for the fixed–ends. Because the initial stability analysis predicts an instability, limit cycles are investigated for a combination of the two lowest frequency modes.

An analysis for an internally resonant system ($\omega_2/\omega_1 = 1^+$) is performed when the KB time averaging method is applied because the frequency ratio is considered to be closely spaced. On the other hand, step by step time integration is used in the same manner regardless of a resonant or non–resonant situation. The rotation of the conductor bundle is found to be very small due to the rigid spacers so that the limiting motions for the windward and leeward conductors are indistinguishable from that at the center of rotation. Therefore, only the limit cycle at the center of rotation is given at the mid–span in Figure 3.5. This figure shows that the results of the step by step time integration procedure and the KB time averaging algorithm agree well. However, the slightly different natural frequencies produced by the two end conditions leads to noticeably different horizontal movements in the limit cycles. The smaller limiting motion amplitude at the fixed ends stems from a higher longitudinal strain (or tension) because the length of the cable changes when one loop galloping happens. However, this change cannot be fed into the adjacent span when the end constraints are fixed.

The change in the peak limit cycle amplitudes at the mid–span is investigated for the simply supported span at various steady wind speeds. The initial stability analysis predicts that the static profile becomes unstable for the first two lowest frequencies when the wind speed exceeds about 2 m/s. It is found, as expected, that the amplitude of the limiting motion grows significantly as the wind speed increases. Indeed, Figure 3.6 shows that the limiting amplitude's growth rate is almost linear and about 10% that of the wind speed. However, the formulation does not accommodate aerodynamic loads that are not weakly–nonlinear at large wind speeds. It has been suggested that a 9 m/s wind speed is at the high end of speeds found to produce galloping [1]. Therefore only 2.5 m/s to 6 m/s wind speeds, which is in the range of moderate winds, are considered here.

Different horizontal static tensions in the conductors cause the change in the limit cycle amplitudes indicated in Figure 3.7. The tensions considered at the 4 m/s wind speed of the example are a little beyond the usual practical range of 15 kN to 30 kN determined from 20% of a conductor's ultimate tensile strength [76]. However, Figure 3.7 shows that, as the tension increases, the limiting motion decreases substantially initially, attains a minimum around 65 kN before rising. This phenomenon can be explained as follows. A larger tension causes the stiffness to increase which, in turn, causes the motion's amplitude to decease but the angular speed to increase. Thus, the aerodynamic forces grow as the static tension increases, as shown in Figure 3.8. (This figure illustrates the dynamic changes during a period of the limiting motion in the aerodynamic coefficients at different static tensions.) Therefore, the motion's amplitude increases when the effect of the aerodynamic forces to inherently increase the cable's motion is greater than the counteracting effect of the tension. Finally, it can be concluded that if galloping is the sole concern, the highest feasible static tension should be employed for this transmission line.

3.4 Concluding Remarks

A nonlinear model has been developed to investigate the full-span oscillations of an iced twin bundle transmission line, the type of oscillations often observed in the field. Numerical solutions involve a finite element analysis employed in conjunction with a perturbation scheme. They account for a line's geometric nonlinearity, pre-stress forces and nonlinear aerodynamic loads. By eliminating the sub-span motions between the two conductors, the twin bundle is modelled as an equivalent single conductor so that the total number of degrees of freedom is halved and computational efficiency is improved greatly. The aerodynamic forces acting on the conductors are obtained from experimental wind tunnel simulations by applying a quasi-steady theory. The initiation of galloping is investigated numerically by using a conventional stability analysis. Limit cycle amplitudes, if oscillations occur, are obtained from an efficient, Krylov-Bogoliubov averaging method and their stability is also studied. In addition, a computationally expedient time marching algorithm is used to compute the response for those instances where averaging procedures cannot be employed. Examples are presented to illustrate typical oscillations of an iced, twin bundle conductor. They suggest that the galloping amplitude grows with increasing wind speed but decreases and, then, increases with a larger horizontal tension.

Calculating the bulk motion of a transmission line is much more computationally efficient than simultaneously considering both full span and sub-span motions because an equivalent single conductor model can be applied. This simpler model can be used for a quick check in a preliminary design of a new transmission line. However, the rotation of iced conductors, which is important in analyzing the limiting motions of single conductors, is suppressed.

Table 3.1: Properties of Field Lines

Parameters	Symbols (Unit)	Data
Conductor diameter	$d\ (m)$	0.0286
Conductor's elasticity modulus	$E\ (N/m^2)$	$4.78033 * 10^{10}$
Torsional rigidity	$GJ\ (N\ m^2/rad)$	101
Axial – torsional coupling parameter	$B_T\ (Nm/rad)$	0
Moment of inertia	$I\ (kg\ m)$	$0.3334 * 10^{-3}$
Eccentricity in y direction	$E_y\ (mm)$	2.05
Eccentricity in z direction	$E_z\ (mm)$	-0.63
Cross–sectional area of conductor	Area (mm^2)	594.48
Area of ice accretion	Area(ice) (mm^2)	423.24
Conductor's mass/unit length	$m\ (kg/m)$	2.379
Damping per unit length in y, z direction	$\xi_y,\ \xi_z$	$0.743 * 10^{-2}$
Damping per unit length in θ direction	ξ_θ	$0.138 * 10^{-2}$
Ice density	(kg/mm^3)	$0.9163 * 10^{-6}$
Distance between two conductors	$l\ (m)$	0.4710
Horizontal span length	$L\ (m)$	125.88
Density of air	$\rho_{air}\ (kg/m^3)$	1.2929
Free stream (wind) speed	$U\ (m/s)$	2.0 – 6.0

Table 3.2: Experimentally Determined Aerodynamic Coefficients

Coefficients	C11 conductor at $\alpha = 0^o$ and $\alpha_W = \alpha_L = 40^o$			
a_{yj}	2.7151,	-0.3335,	-8.1094,	16.7162
a_{zj}	1.7440,	1.7210,	1.6650,	3.56309
$a_{\theta j}$	0.3206,	-1.4543,	0.5869,	11.9408
$j = 0, 1, 2, 3$				

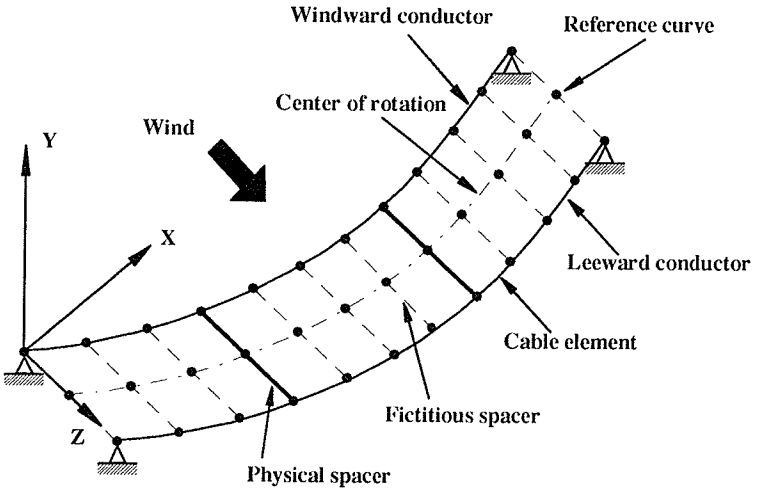

Figure 3.1: Bulk modelling of a twin bundle conductor

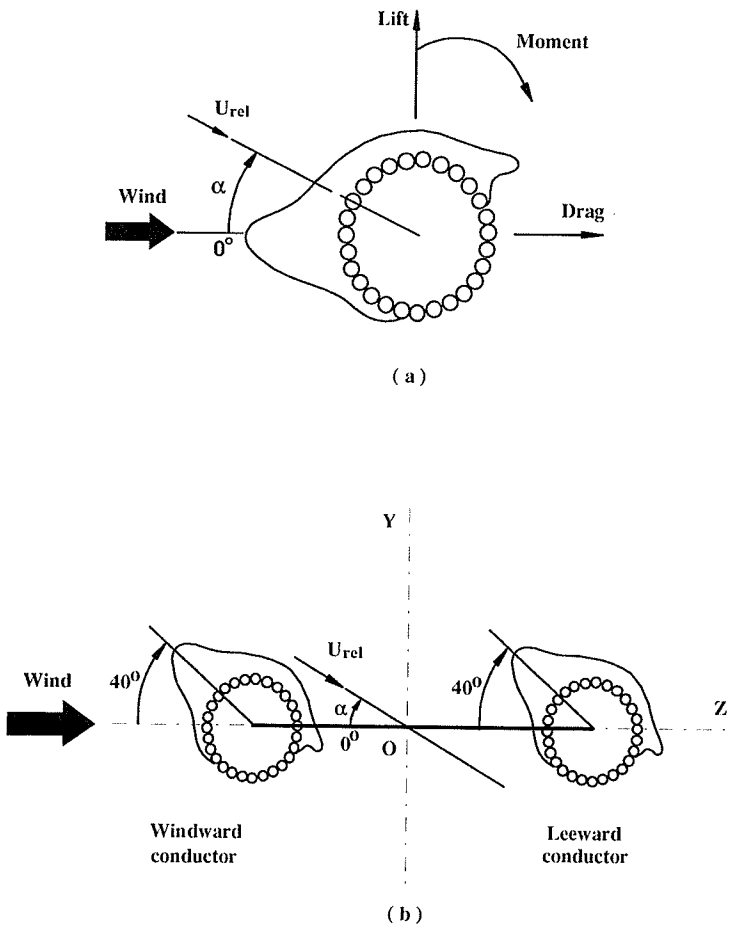

Figure 3.2: The twin bundle model showing (a) the cross–section of a single C11 conductor and (b) the arrangement of the windward and leeward conductors

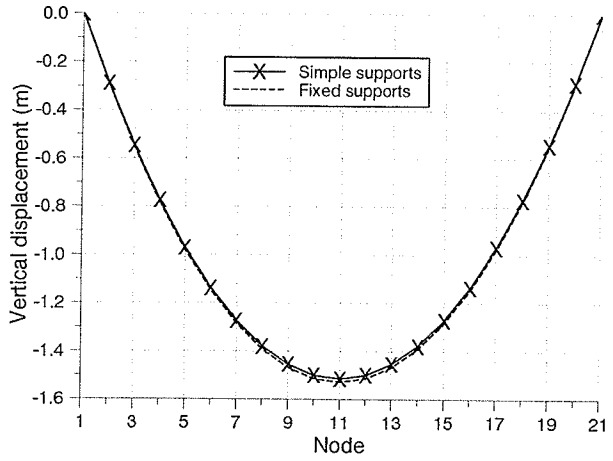

(a)

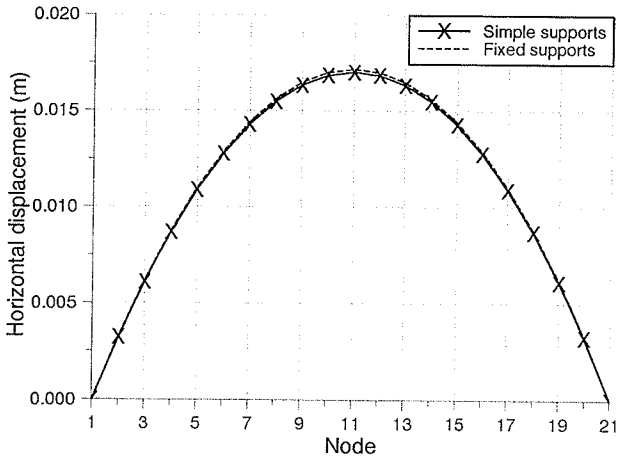

(b)

Figure 3.3: The span's static profile in the (a) vertical and (b) horizontal directions

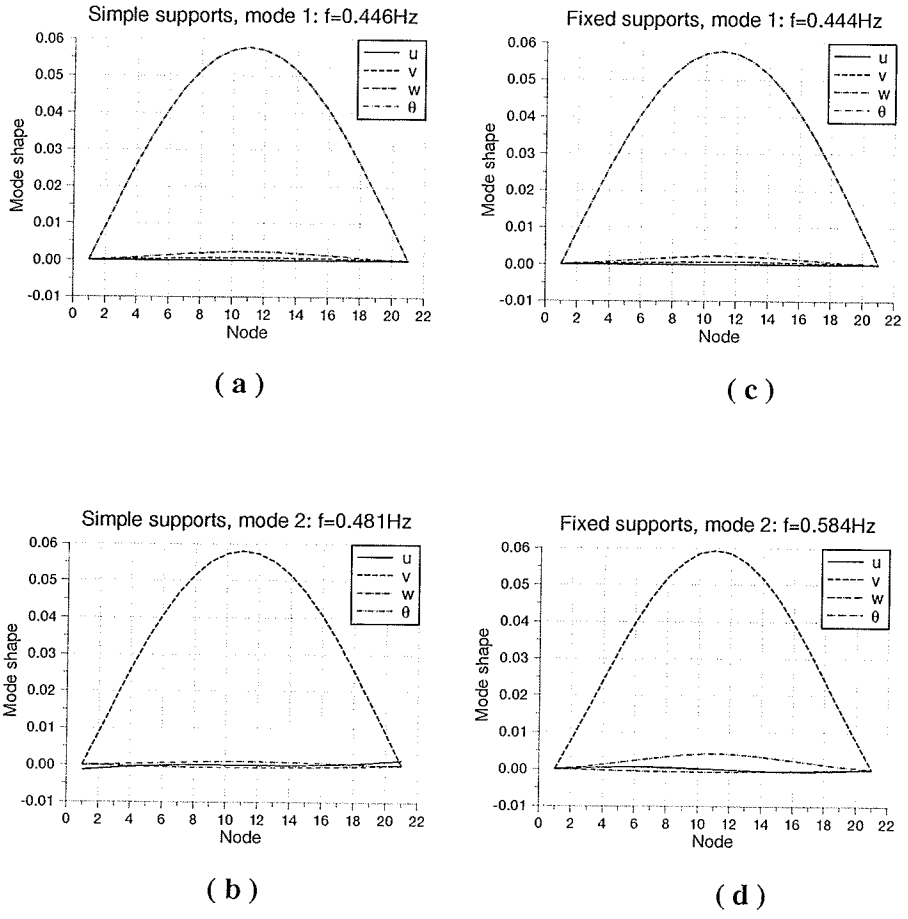

Figure 3.4: Lowest two frequency, single loop, symmetrical mode shapes for (a) and (b) simply supported ends; and (c) and (d) fixed ends

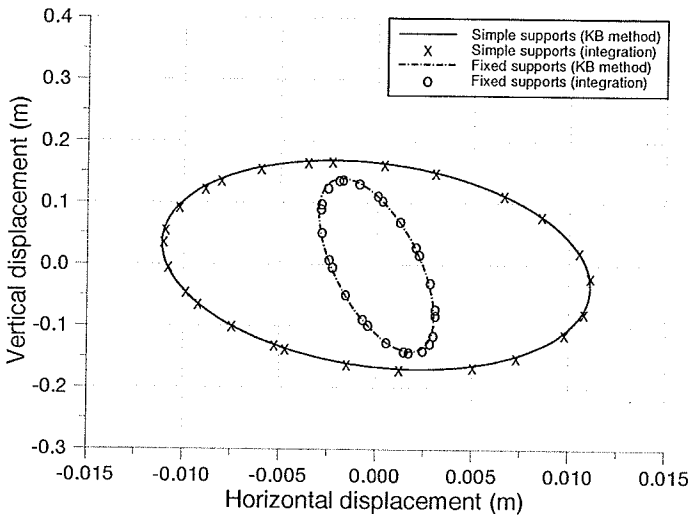

Figure 3.5: Limit cycle loci obtained at the mid–span by using the KB method and direct numerical integration

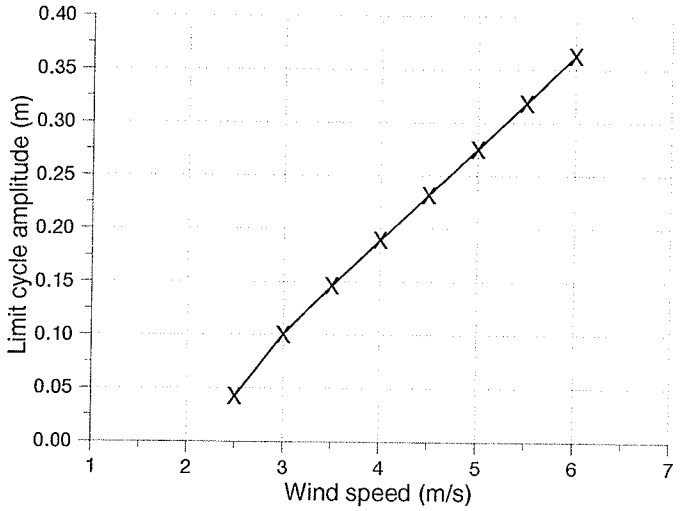

Figure 3.6: Amplitude of midspan's limiting motion with increasing wind speed

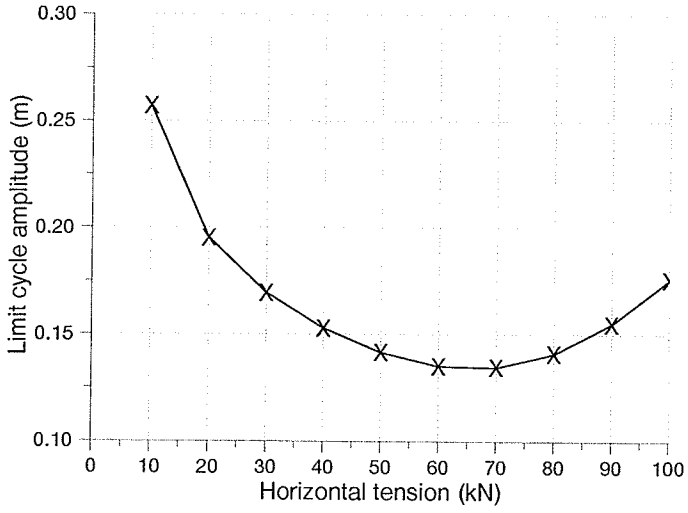

Figure 3.7: Amplitude of midspan's limiting motion with changing horizontal tension

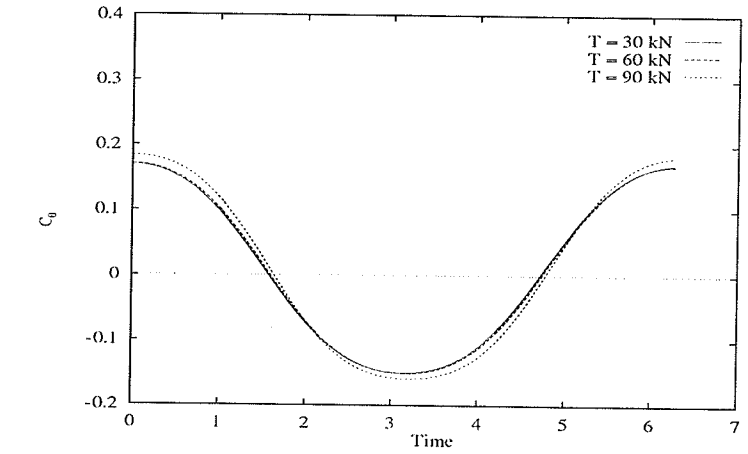

(a)

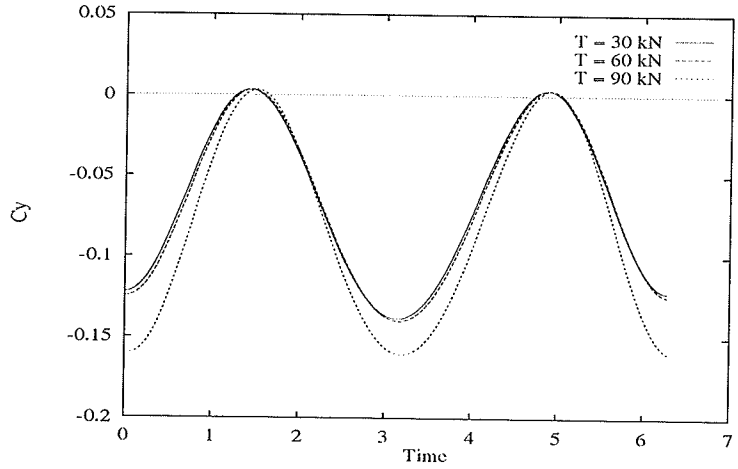

(b)

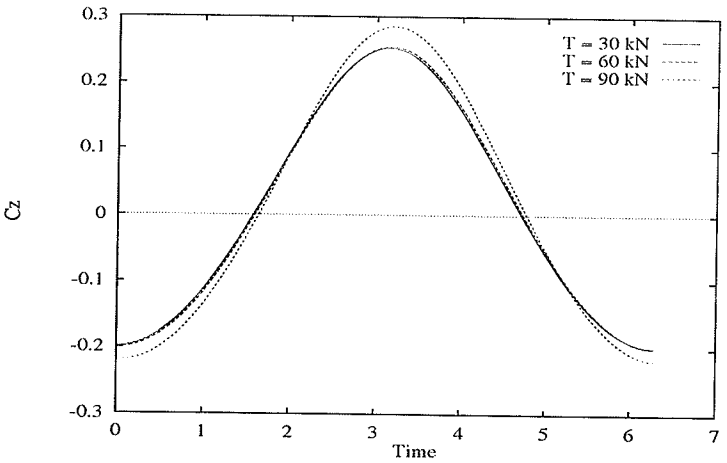

(c)

Figure 3.8: Coefficients of the aerodynamic forces in a period of the limiting motion

Chapter 4

Wake–Induced Oscillations

4.1 Introduction

The equivalent single conductor model described in Chapter 3 efficiently computes the full span motion of a twin conductor bundle. However, modelling galloping or wake–induced oscillations becomes necessary when sub–span motions are not negligible. Investigations of wake effects on bare conductors have been performed by considering two circular cylinders, one in the wake of the other. In one set of investigations, the windward cylinder was fixed and the leeward cylinder was suspended by a spring and a dashpot. A single degree of freedom (DOF) oscillator, involving vertical motion [4], and a two DOF model, accommodating both the horizontal and vertical motions [5, 7, 41], have been employed to find the limit cycle of the leeward cylinder. The computational superiority of a time averaging method, commonly the Krylov-Bogoliubov (KB) method, has been illustrated for those oscillator models for which periodic limiting motions and their stability conditions were determined explicitly [4, 7, 41].

When the windward cylinder is free to move and both cylinders are represented by masses supported by springs and dampers, a four DOF oscillator model is needed [6, 77]. The resulting nonlinear equations of motion have been integrated numerically by utilizing a time marching scheme. Unfortunately, such a scheme may be very time consuming, especially for a lightly damped system when many oscillation cycles

have to be performed before a limiting periodic or quasi-periodic dynamic response is attained.

This chapter studies low frequency vibrations, including both the galloping of an individual conductor and the wake-induced oscillations of twin-bundle conductors coated with ice and subjected to a steady side wind. The aerodynamic forces needed for the analyses are obtained from static wind tunnel measurements by assuming that a quasi-steady theory is valid for low frequency motions. A finite element analysis, as well as a perturbation scheme, are employed to derive and solve the nonlinear equations. The finite element model takes into account both a full span and a subspan motion and it is able to accommodate non-uniform ice geometries and wind loads along a continuous line. Three-node, isoparametric cable elements are used to account for the conductor's geometrical nonlinearity, whilst two-node beam elements represent the relatively rigid spacers. A D–section is a typical ice shape of extreme icing found in field observations and freezing rain simulations [78]. Therefore, the aerodynamic data for the D–section are used in the numerical experimentation. The initiation of galloping, the limiting amplitude, if galloping occurs, as well as the history of a twin–bundle transmission line's motion are investigated. Results for twin conductors having different degrees of structural coupling are also presented.

4.2 General formulation

The finite element method employed to analyze the galloping of a twin-bundle transmission line utilizes three-node isoparametric cable elements for the conductors [67] and two node beam elements for the spacers spanning the two nearby conductors

[79]. The equations of motion,

$$[M]\{\ddot{q}\} + [C]\{\dot{q}\} + [K]\{q\} = \{F\}, \tag{4.1}$$

are derived from the static configuration of the transmission line by employing a variational principle [80]. The $[M]$, $[C]$ and $[K]$ are the global $N \times N$ structural mass, damping and stiffness matrices, respectively. The $\{q\}$ and $\{F\}$, on the other hand, are the global displacement and external dynamic load vectors, respectively. The ice on the conductor is taken into consideration when forming $[M]$ and $[K]$. The effects of remote spans and support insulator strings are represented by linear springs and they are reflected in the stiffness matrix, $[K]$. It should be noted that the $[K]$ and $\{F\}$ are nonlinear functions of $\{q\}$ or $\{\dot{q}\}$. The basic formulation for the elements' mass, damping and stiffness matrices as well as the external force vectors is summarized in the following subsections. Further details and the explicit forms can be found in reference [81].

4.2.1 Elements

The three node cable and two node beam elements that are used to idealize conductors and spacers are described in Appendix A. Explicit expressions for the mass and stiffness matrices are given in Appendix B.

4.2.2 Remote spans and support-insulator strings

Remote spans are modelled as weightless linear springs having stiffness, K_{ST}, in the global X direction as shown in Figure 1.1. The K_{ST} is added to the diagonal entry in the global stiffness matrix, $[K]$, which corresponds to the U displacement at a tower hardware's simple support connection to a conductor. The support insulator

string, which is considered to be a single, vertical rigid bar, pin connected to the tower's arm, is also modelled as a linear static spring having components K_{Ix} and K_{Iz} in the X and Z directions, respectively. The K_{Ix} affects the diagonal stiffness term associated with the corresponding U displacement whereas K_{Iz} contributes to the analogous term associated with the W displacement. Details can be found in Appendix C.

4.2.3 Damping matrix

The determination of an element's damping matrix, $[C^e]$, is difficult in practice because of incomplete experimental data. It is often assumed, therefore, that the global structural damping matrix, $[C]$, can be approximated by Rayleigh damping, which is a linear combination of the stiffness and mass matrices, i.e.

$$[C] \;=\; \beta_1\,[M] \;+\; \beta_2\,[K], \tag{4.2}$$

where β_1 and β_2 are determined experimentally. Details can be found in Appendix D.

4.2.4 Aerodynamic forces

The aerodynamic forces, which cause the conductor to vibrate, depend nonlinearly upon the geometry of the iced conductors and the relative wind velocities to the conductors. The force vector, $\{F\}$, in equation (4.1) is formulated in the global coordinate system. It is evaluated by measuring the quasi-steady lift, F_L, drag, F_D, and moment, M_θ. In general, the aerodynamic forces per unit length can be written at each nodal point in the form

$$F_L \;=\; \frac{1}{2}\,\rho_{air}\,U_R^2\,d\,C_L,$$

$$F_D = \frac{1}{2}\,\rho_{air}\,U_R^2\,d\,C_D, \tag{4.3}$$

and

$$M_\theta = \frac{1}{2}\,\rho_{air}\,U_R^2\,d^2\,C_\theta,$$

where ρ_{air}, U_R, d and C_i, $i = L, D, \theta$, are the density of the air, relative wind speed with respect to a conductor, diameter of a bare conductor and the lift, drag and moment coefficients, respectively. It has been found experimentally that C_L, C_D and C_θ have different forms for windward and leeward conductors. Therefore, the forces on these conductors need to be treated individually.

Wind tunnel measurements

Aerodynamic forces and moments are measured on both windward and leeward conductor samples in static wind tunnel tests for different orientations and various locations of the leeward conductor in the wake of the windward one [78]. Ice shapes are generated on the conductors in freezing rain simulations that duplicate the meteorological conditions for naturally occurring freezing rain. After validating several simulated ice shapes by comparing them with much more difficult to obtain natural ice profiles formed under comparable conditions, short models representing the most commonly encounted or severest ice shapes are used for wind tunnel testing. The location and orientation of the models are constrained to the four geometric degrees of freedom sketched in Figure 4.1(a). The Z and Y are the horizontal and vertical separations between the models' centers and α_W and α_L are the angles of incidence of the free air stream to the windward and leeward models about their geometrical centers of rotations, respectively. Least square curve fitting is used for the measured force coefficients C_L, C_D and C_θ to obtain smooth curves for a theoretical analysis.

Windward conductor

Aerodynamic forces and moment depend nonlinearly upon the geometry of the iced conductor, the relative wind speed, U_R, and the relative angle of the wind to the conductor, α. The U_R and α for the windward conductor are expressed, at a typical iced cross section, by [1]

$$U_{RW}^2 = (U - \dot{Z}_W)^2 + \dot{Y}_W^2$$

and

$$\alpha_W = \theta_W - \alpha_{WV} \tag{4.4}$$

where U is the free stream speed. Subscript, W, indicates a variable related to the windward conductor here and in the sequel to avoid repetition, e.g. U_{RW} is the wake speed relative to the windward conductor. Also,

$$\alpha_{WV} = tan^{-1}(\frac{\dot{Y}_W}{U - \dot{Z}_W}) \tag{4.5}$$

$$\dot{Y}_W = \dot{V}_W + R_W\dot{\theta_W}$$

and

$$\dot{Z}_W = \dot{W}_W, \tag{4.6}$$

where R_W is a characteristic radius corresponding to a reference point where the instantaneous angle of attack, α_W, is computed. This reference point is presumed to be located at the windward sides of both individual conductors so that R_W (and R_L) is approximately $d/2$.

The C_L, C_D and C_θ for the windward conductor depend nonlinearly upon the relative angle of the wind's attack on the conductor, α_W. If the structural rotation is assumed small, the forces F_y and F_z and the moment M_θ in the xyz coordinate system can be approximated by [1]

$$F_y \doteq F_L(\alpha_W)\cos\alpha_W + F_D(\alpha_W)\sin\alpha_W,$$

$$F_z \doteq -F_L(\alpha_W)\sin\alpha_W + F_D(\alpha_W)\cos\alpha_W, \tag{4.7}$$

and

$$M_\theta \doteq M_\theta(\alpha_W).$$

Hence, the substitution of equation (4.3) into equations (4.7) results in

$$\begin{aligned} F_y &\doteq \frac{1}{2}\,\rho_{air}\,[U^2 + (R_W\dot{\theta}_W + \dot{V}_W)^2]\; d\; C_y(\alpha_W), \\ F_z &\doteq \frac{1}{2}\,\rho_{air}\,[U^2 + (R_W\dot{\theta}_W + \dot{V}_W)^2]\; d\; C_z(\alpha_W), \end{aligned} \tag{4.8}$$

and

$$M_\theta \doteq \frac{1}{2}\,\rho_{air}\,[U^2 + (R_W\dot{\theta}_W + \dot{V}_W)^2]\; d^2\; C_\theta(\alpha_W).$$

The C_L, C_D and C_θ are determined from quasi-steady, wind tunnel experiments on single conductors [78] and they are utilized to compute the C_y, C_z and C_θ of equation (4.8). The angle of attack to the windward conductor, α_W, is scaled such that $\alpha_W = 0$ at the static equilibrium position of the windward conductor. In the present analysis, the cubic polynomials

$$C_i = \sum_{j=1}^{3} a_{ij}\;\alpha_W^j, \qquad i = y, z, \theta \tag{4.9}$$

are employed to represent the experimental results. The approximation described in section 3.2.2 of Chapter 3, viz

$$\alpha_W = \overline{\alpha}_W + \tilde{\alpha}_W^3/3, \tag{4.10}$$

where

$$\begin{aligned} \overline{\alpha}_W &= \theta_W - \tilde{\alpha}_W \\ \tilde{\alpha}_W &= (R_W\dot{\theta}_W + \dot{v}_W)/U \end{aligned} \tag{4.11}$$

is used in the time averaging process. The a_{ij}, $j = 0, 1, 2, 3$ and $i = y, z, \theta$, of equation (4.9) are obtained from a least square curve fit of experimental data. The constant term a_{i0} in equation (4.9) is omitted in the time integration process and the computation of the limit cycle because it is absorbed in the formation of the static loads.

Leeward conductor

The aerodynamic forces acting on the leeward conductor, which are produced by the wake of the windward conductor, depend nonlinearly upon the relative positions (Y and Z) and rotations (α_W and α_L) of the two conductors. Usually the motion of the windward conductor affects the leeward conductor after a time delay due to the retardation of the wake flow leaving the windward conductor and approaching the leeward conductor [82]. However, this flow retardation is neglected here because galloping happens at a low frequency. Hence, the motion of the windward conductor can be considered 'small' because its speed is much less than that of either the free or wake stream . If the time delay is included, a similar procedure to that given below can also be used.

The general form of the aerodynamic forces acting on the leeward conductor in the xyz coordinate system is similar to that on the windward conductor which is described in equation (4.7). The forces and moment can be obtained again by applying the quasi-steady assumption so that

$$\begin{aligned} F_y &= \frac{1}{2}\,\rho_{air}\,U_{RL}^2\,d\,(-\overline{C}_D \sin\alpha_{LV} + \overline{C}_L \cos\alpha_{LV}) \\ F_z &= \frac{1}{2}\,\rho_{air}\,U_{RL}^2\,d\,(\overline{C}_D \cos\alpha_{LV} + \overline{C}_L \sin\alpha_{LV}) \end{aligned} \tag{4.12}$$

and

$$M_\theta = \frac{1}{2}\,\rho_{air}\,U_{RL}^2\,d^2\,\overline{C}_\theta.$$

Here U_{RL} is the wake's speed relative to the leeward conductor, whilst $\alpha_{LV} = \theta_L - \alpha_L$ where θ_L and α_L are the rotation and flow angle of the wind's attack on the leeward conductor. The lift, drag and moment coefficients on the leeward conductor, $\overline{C}_L$, $\overline{C}_D$ and $\overline{C}_\theta$, may be expressed in terms of C_L, C_D and C_θ by using [6]

$$\overline{C}_D = C_D/b^2, \quad \overline{C}_L = C_L/b^2 \quad \text{and} \quad \overline{C}_\theta = C_\theta/b^2,$$

where $b = (C_D/C_{D_\infty})^{1/2}$ is the ratio of the wake to the free stream airspeed. The C_L, C_D and C_θ are based on the free stream airspeed and they are obtained experimentally by employing a static model. If bare conductors or circular cylinders are used, these coefficients depend nonlinearly on the relative position between the two conductors [5, 7]. However, the coefficients are functions of the relative wind angle as well as relative position when the conductors are covered with ice. They can be written in the form

$$C_i = C_i(\alpha_W, \alpha_L, Y', Z'), \qquad C_i = C_L, C_D, C_\theta, \tag{4.13}$$

where Y' and Z' are the separations between the two conductors in the Y' and Z' directions, respectively, as shown in Figure 4.1(b).

By using the definition of b, the resultant wake velocity relative to the windward conductor, $\vec{U}_W$ can be seen from Figure 4.2 to be

$$\vec{U}_W = b\,\vec{U}_{RW}, \tag{4.14}$$

where $\vec{U}_{RW}$ is the wind velocity relative to the windward conductor. The absolute wake velocity components are derived, by utilizing equation (4.14), to be

$$U_{WY} = b\,U_{RW}\,\sin\alpha_{WV} - \dot{Y}_W$$

$$U_{WZ} = b\, U_{RW}\ \cos\alpha_{WV} + \dot{Z}_W, \tag{4.15}$$

where

$$\dot{Y}_W = \dot{V}_W\ +\ R_W\,\dot{\theta}_W$$

$$\dot{Z}_W = \dot{W}_W$$

$$\alpha_{WV} = \tan^{-1}(\frac{\dot{Y}_W}{U - \dot{Z}_W})$$

and

$$\alpha_W = \theta_W - \alpha_{WV}.$$

Hence, the components of the wake velocity relative to the leeward conductor can be written as

$$U_{LY} = b\, U_{RW}\ \sin\alpha_{WV} - \dot{Y}_W + \dot{Y}_L$$

$$U_{LZ} = b\, U_{RW}\ \cos\alpha_{WV} + \dot{Z}_W - \dot{Z}_L, \tag{4.16}$$

where

$$\dot{Y}_L = \dot{V}_L\ +\ R_L\,\dot{\theta}_L$$

and

$$\dot{Z}_L = \dot{W}_L.$$

Simplifying equation (4.16) by including only first order terms gives

$$U_{LY} = b\,\dot{Y}_W - \dot{Y}_W + \dot{Y}_L$$

and

$$U_{LZ} = b\,(U - \dot{Z}_W) + \dot{Z}_W - \dot{Z}_L. \tag{4.17}$$

Then the U_{RL} and α_{LV} given in equation (4.12) can be found to be

$$U_{RL}^2 = U_{LY}^2 + U_{LZ}^2 \tag{4.18}$$

and

$$\alpha_{LV} = \tan^{-1}(U_{LY}/U_{LZ}) \tag{4.19}$$

when the angle of attack, α_L, used in equation (4.13), is defined by

$$\alpha_L = \theta_L - \alpha_{LV}. \tag{4.20}$$

By substituting equation (4.18) into equation (4.12) and applying a similar approximation to that used for equation (4.7), the aerodynamic forces can be written in the form

$$\begin{aligned} F_y &\doteq \frac{1}{2}\, d\, \rho_{air}\, U_e^2\, C_y(\alpha_W, \alpha_L, y, z), \\ F_z &\doteq \frac{1}{2}\, d\, \rho_{air}\, U_e^2\, C_z(\alpha_W, \alpha_L, y, z), \\ M_\theta &\doteq \frac{1}{2}\, d^2\, \rho_{air}\, U_e^2\, C_\theta(\alpha_W, \alpha_L, y, z), \end{aligned} \tag{4.21}$$

where

$$U_e^2 = U^2 \left\{ \left[1 + \frac{(1-b)\dot{Z}_W - \dot{Z}_L}{bU} \right]^2 + \left[\frac{(1-b)\dot{Y}_W - \dot{Y}_L}{bU} \right]^2 \right\}.$$

In this analysis, the force coefficient C_y is approximated by

$$\begin{aligned} C_y = {} & \sum_{k=0}^{4}(B_{k,1} + B_{k,2}z)y^k + \alpha_W(\sum_{k=0}^{4} B_{k,3}y^k + \sum_{k=0}^{3} B_{k,4}zy^k) \\ & +\alpha_L(\sum_{k=0}^{4} B_{k,5}y^k + \sum_{k=0}^{3} B_{k,6}zy^k) + \alpha_W^2(\sum_{k=0}^{3} B_{k,7}y^k + \sum_{k=0}^{2} B_{k,8}zy^k) \\ & +\alpha_W\alpha_L(\sum_{k=0}^{3} B_{k,9}y^k + \sum_{k=0}^{2} B_{k,10}zy^k) + \alpha_L^2(\sum_{k=0}^{3} B_{k,11}y^k + \sum_{k=0}^{2} B_{k,12}zy^k) \\ & +\alpha_W^3(\sum_{k=0}^{2} B_{k,13}y^k + \sum_{k=0}^{1} B_{k,14}zy^k) + \alpha_W^2\alpha_L(\sum_{k=0}^{2} B_{k,15}y^k + \sum_{k=0}^{1} B_{k,16}zy^k) \\ & +\alpha_W\alpha_L^2(\sum_{k=0}^{2} B_{k,17}y^k + \sum_{k=0}^{1} B_{k,18}zy^k) + \alpha_L^3(\sum_{k=0}^{2} B_{k,19}y^k + \sum_{k=0}^{1} B_{k,20}zy^k). \end{aligned} \tag{4.22}$$

Similar approximations are made for C_z and C_θ which have coefficients $C_{k,i}$ and $D_{k,i}$, respectively, and possess the same ranges for k and i as those for $B_{k,i}$. These coefficients are all obtained from curve fitting experimental data. On the other

hand, the variables y and z employed in the last equation are shown schematically in Figure 4.1(b). They are defined as

$$\begin{aligned} y &= Y' - y_0 \\ z &= Z' - z_0, \end{aligned} \tag{4.23}$$

where y_0 and z_0 are the relative separations of the two conductors at the static equilibrium position in the y and z directions, respectively. Hence

$$\begin{aligned} Y' &= \overline{Y}\cos\alpha_{WV} + \overline{Z}\sin\alpha_{WV} \\ Z' &= -\overline{Y}\sin\alpha_{WV} + \overline{Z}\cos\alpha_{WV}, \end{aligned} \tag{4.24}$$

and

$$\begin{aligned} \overline{Y} &= Y_B + V_L - V_W \\ \overline{Z} &= Z_B + W_L - W_W \end{aligned} \tag{4.25}$$

where V_L, V_W, W_L and W_W are the displacement components of the leeward and windward conductors in the Y and Z directions, respectively. The Y_B and Z_B are the initial separations of the conductors in the Y and Z directions, respectively.

4.2.5 Initiation of Galloping

The static configuration of a transmission line, subjected to loads from ice and a mean steady side wind, is found by solving the nonlinear static equilibrium equations stemming from letting $\{\dot{q}\} = \{\ddot{q}\} = 0$ in equation (4.1). The resulting nonlinear static equations,

$$[K]\{q\} = \{F\}, \tag{4.26}$$

are solved by using the NR iteration method described in section 2.2.1 of Chapter 2. The initiation of galloping is determined by the stability of the static equilibrium

configuration of the transmission line. The static configuration is stable if all the eigenvalues of the characteristic matrix, $[S_c]$, determined in equation (2.17) have a negative real part. If the static configuration is unstable, the limiting motion and the history of a motion are found by employing two independent methods, the KB averaging scheme and direct time integration.

4.2.6 Limit cycles

By considering the equations of motion to be weakly nonlinear, time averaging schemes can be used to approximate the periodic and quasi-periodic solutions. The equations of motion (4.1) are transformed first to the principal coordinate system, η_i, as [1]

$$\ddot{\eta}_i + \omega_i^2 \eta_i = F_{\eta_i} - \sum_{k=1}^{N_p} c^*_{i,k} \dot{\eta}_k, \qquad i = 1, 2, \ldots, N_p, \tag{4.27}$$

where

$$F_{\eta_i} = \sum_{j=1}^{n_p} (\phi_{4j-2,i}\ F_{y_j} + \phi_{4j-1,i}\ F_{z_j} + \phi_{4j,i}\ M_{\theta_j}).$$

Here n_p and N_p are the number of nodal points and principal coordinates, respectively. The ω_i^2, $\phi_{i,j}$, F_{η_i} and $c^*_{i,k}$, on the other hand, are the squared natural frequencies, elements of the eigenfunction matrix $[\phi]$, forcing vector $\{F^*\}$ and damping matrix $[C^*]$ in the principal coordinate system, respectively. Then the KB technique is applied to the modified equations

$$\ddot{\eta}_i + \omega^{*2}_i \eta_i = F_{\eta_i} - \sum_{k=1}^{N_p} c^*_{i,k} \dot{\eta}_k + (\omega^{*2}_i - \omega_i^2)\eta_i, \qquad i = 1, 2, \ldots, N_p, \tag{4.28}$$

as described in equation (2.6) of Chapter 2. The resulting $2N_p$ averaged equations (2.9) and (2.10) become

$$\overline{\dot{A}_i \omega_i^*} = \overline{F}_{A_i} = \lim_{T \to \infty} \frac{1}{T} \int_0^T [A_i(\omega_i^2 - \omega_i^{*2}) cos\Psi_i - F_{\eta_i} - F_{c_i}] sin\Psi_i dt \tag{4.29}$$

and

$$\overline{A_i\dot{\psi}_i\omega_i^*} = \overline{F}_{\psi_i} = \lim_{T\to\infty}\frac{1}{T}\int_0^T [A_i(\omega_i^2 - \omega_i^{*2})cos\Psi_i - F_{\eta_i} - F_{c_i}]cos\Psi_i dt, \tag{4.30}$$

where

$$F_{c_i} = \sum_{k=1}^{N_p} c_{i,k}^*\ A_k\ \omega_k^*\ \sin\Psi_k. \tag{4.31}$$

By substituting equation (4.31) into equations (4.29) and (4.30), the expressions

$$\begin{aligned}\overline{F}_{A_i} \;=\; -\lim_{T\to\infty}\frac{1}{T}\int_0^T \left[\sum_{j=1}^{n_p} F_{yz\theta}^j\right]\ \sin\Psi_i\ dt - \sum_{k=1}^{N_p}\frac{\delta_{ik}}{2}c_{i,k}^*\ \overline{A}_k\ \omega_k^*\ \cos\overline{\psi}_{ki} \\ ,i = 1,2,\ldots,N_p\end{aligned} \tag{4.32}$$

and

$$\begin{aligned}\overline{F}_{\psi_i} \;=\; -\lim_{T\to\infty}\frac{1}{T}\int_0^T \left[\sum_{j=1}^{n_p} F_{yz\theta}^j\right]\ \cos\Psi_i dt - \sum_{k=1}^{N_p}\frac{\delta_{ik}}{2}c_{i,k}^*\ \overline{A}_k\ \omega_k^*\ \sin\overline{\psi}_{ki} \\ +\frac{\overline{A}_i}{2}(\omega_i^2 - \omega_i^{*2}) \qquad\qquad ,i = 1,2,\ldots,N_p\end{aligned} \tag{4.33}$$

are formed where $F_{yz\theta}^j$, which corresponds to the principal coordinate η_i at nodal point j, is defined as

$$F_{yz\theta}^j \;=\; \phi_{4j-2,i}\ F_{y_j} + \phi_{4j-1,i}\ F_{z_j} + \phi_{4j,i}\ M_{\theta_j}\ . \tag{4.34}$$

The phase difference, $\overline{\psi}_{ki}$, and function, δ_{ik}, are given by

$$\overline{\psi}_{ki} \;=\; \overline{\psi}_k \;-\; \overline{\psi}_i\ , \tag{4.35}$$

and

$$\delta_{ik} \;=\; \begin{cases} 1 & \text{if}\ \ \omega_i^* \;=\; \omega_k^* \\ 0 & \text{if}\ \ \omega_i^* \;\neq\; \omega_k^*\ . \end{cases} \tag{4.36}$$

The aerodynamic forces on the windward and leeward conductors have different forms and, therefore, they are treated separately next. The nodal numbers are

arranged, for convenience, such that odd (even) numbers are on the windward (leeward) conductor and consecutive numbers increase by two from the left to the right end support.

Nodal points on windward conductor

When j is an odd nodal number, equation (4.34) becomes

$$F^j_{yz\theta} = \frac{1}{2}\rho_{air}\ \{{U_{zj}}^2 + (R_{Wj}\dot{\theta}_{Wj})^2\}\ d_j\ \left(\sum_{k=1}^{3} \overline{a}_k\ \alpha^k_{Wj}\right), \tag{4.37}$$

where

$$\overline{a}_p = \phi_{(4j-2),i}\ \overline{a}_{yp} + \phi_{(4j-1),i}\ \overline{a}_{zp} + \phi_{4j,i}\ \overline{a}_{\theta p}\ d_j \quad , p = 1, 2, 3. \tag{4.38}$$

After further algebraic manipulation, equation (4.37) becomes

$$F^j_{yz\theta} = \frac{1}{2}\ \rho_{air}\ {U_{zj}}^2\ d_j\ \left(\sum_{k=1}^{3} \overline{a}_k\ \overline{\alpha}^k_{Wj} + \delta_\alpha\ \overline{a}_1\ \tilde{\alpha}^3_{Wj}/3\ + \delta_\alpha\ \overline{a}_1\ \overline{\alpha}_{Wj}\tilde{\alpha}^2_{Wj}\ \right), \tag{4.39}$$

where

$$\delta_\alpha = \begin{cases} 1 & \text{if } \tilde{\alpha}_W \text{ is considered large ,} \\ 0 & \text{if } \tilde{\alpha}_W \text{ is considered small .} \end{cases} \tag{4.40}$$

Here $\tilde{\alpha}_W$ is considered small when $\tilde{\alpha}_W << 0.1$ so that the linear approximation given by equation (4.10) is valid. The U_{zj}, d_j and θ_{Wj} are the steady free air speed, a reference structural dimension and the windward conductor's rotation at the jth node, respectively. On the other hand, $\overline{A}_i$ and $\overline{\psi}_i$ indicate the time averaged amplitude and the time shift, respectively, of the ith mode. The $\overline{a}_{yp}$, $\overline{a}_{zp}$ and $\overline{a}_{\theta p}$ are computed from

$$\overline{a}_{kp} = \left(\frac{L_m + L_n}{4}\right)\ a_{kp} \quad ;\ k = y, z, \theta\ ;\ p = 1, 2, 3\ ;\ j = 1, 3, \ldots, n_p - 1\ , \tag{4.41}$$

where L_m and L_n are the lengths of the adjacent mth and nth elements, respectively, to which j ($(j+1)/2 \neq 2, 4, 6, \ldots$) is the common node. If $(j+1)/2 = 2, 4, 6, \ldots$,

then $L_m = L_n = L_e$ is the length of the element for which j is the middle node. The $\overline{\alpha}_j$ and $\tilde{\alpha}_j$ in equation (4.39) are simplified further to the form

$$\overline{\alpha}_j = \sum_{n=1}^{N_p} \left(C_n^j \cos \Psi_n + S_n^j \sin \Psi_n \right) \tag{4.42}$$

$$\tilde{\alpha}_j = - \sum_{n=1}^{N_p} S_n^j \sin \Psi_n \quad , \tag{4.43}$$

where

$$\begin{aligned} C_n^j &= \overline{A}_n \, \phi_{4j,n} \\ S_n^j &= \frac{\overline{A}_n \omega_n^*}{U_{zj}} \left(R_j \, \phi_{4j,n} + \phi_{(4j-2),n} \right) \quad . \end{aligned} \tag{4.44}$$

The R_j in the last equation represents the characteristic radius at the jth node and $\phi_{i,j}$ is the ijth element of $[\phi]$.

It can be seen from equations (4.32), (4.33), (4.37) and (4.42) that the infinite integration of the products of terms linear, quadratic and cubic in $\overline{\alpha}_j$ as well as linear in θ_j, that are associated with $\sin \Psi_i$ and $\cos \Psi_i$, are required recursively at each jth node, for every ith mode. These integrations have been derived explicitly but they are not presented here for brevity. Details can be found in reference [1].

Nodal points on leeward conductor

When j is an even nodal number, equation(4.34) becomes

$$\begin{aligned} F_{yz\theta}^j = \frac{1}{2} \rho_{air} d_j {U_{zj}}^2 \Bigg\{ & \left[1 + (1-b) \frac{\dot{W}_W}{bU} - \frac{\dot{W}_L}{bU} \right]^2 \\ & + \left[-\frac{1-b}{bU} (\dot{V}_W + R_W \dot{\theta}_W) + \frac{1}{bU} (\dot{V}_L + R_L \dot{\theta} L) \right]^2 \Bigg\} C_{yz\theta}^j, \end{aligned} \tag{4.45}$$

where

$$C_{yz\theta}^j = \phi_{(4j-2),i} \, C_{yj} + \phi_{(4j-1),i} \, C_{zj} + \phi_{4j,i} \, C_{\theta j} \, d_j \; . \tag{4.46}$$

The C_{yj}, C_{zj} and $C_{\theta j}$, which are defined in equation (4.22), can be simplified further by using

$$
\begin{aligned}
y &\doteq V_L - V_W + z_0 \frac{R_W}{U}\dot{\theta}_W + z_0 \frac{1}{U}\dot{V}_W, && (4.47)\\
z &\doteq W_L - W_W - y_0 \frac{R_W}{U}\dot{\theta}_W - y_0 \frac{1}{U}\dot{V}_W, && (4.48)\\
\alpha_W &\doteq \theta_W - \frac{R_W}{U}\dot{\theta}_W - \frac{1}{U}C\dot{V}_W, && (4.49)\\
\alpha_L &\doteq \theta_L - \frac{R_L}{bU}\dot{\theta}_L - \frac{1}{bU}\dot{V}_L + \frac{1-b}{bU}R_W\dot{\theta}_W + \frac{1-b}{bU}\dot{V}_W. && (4.50)
\end{aligned}
$$

Therefore,

$$
\begin{aligned}
F^j_{yz\theta} &= \frac{1}{2}\rho_{air}\ d_j\ {U_{zj}}^2 \left\{ \left[1 + \sum_{k=1}^{N_p} G_{1,k} \sin\Psi_k \right]^2 + \left[\sum_{k=1}^{N_p} G_{2,k} \sin\Psi_k \right]^2 \right\} C^j_{yz\theta}, && (4.51)\\
y_j &= \sum_{k=1}^{N_p} G_{3,k} \cos\Psi_k + \frac{z_0}{U} \sum_{k=1}^{N_p} G_{4,k} \sin\Psi_k, && (4.52)\\
z_j &= \sum_{k=1}^{N_p} G_{5,k} \cos\Psi_k - \frac{y_0}{U} \sum_{k=1}^{N_p} G_{4,k} \sin\Psi_k, && (4.53)\\
\alpha_{wj} &= \sum_{k=1}^{N_p} G_{6,k} \cos\Psi_k - \frac{1}{U} \sum_{k=1}^{N_p} G_{7,k} \sin\Psi_k, && (4.54)\\
\alpha_{Lj} &= \sum_{k=1}^{N_p} G_{8,k} \cos\Psi_k - \frac{1}{bU} \sum_{k=1}^{N_p} G_{9,k} \sin\Psi_k, && (4.55)
\end{aligned}
$$

where

$$
\begin{aligned}
G_{1,k} &= (-\overline{A}_k\omega^*_k) \left(\frac{1-b}{bU}\ \phi_{4(j-1)-1,k} - \frac{1}{bU}\ \phi_{4j-1,k} \right),\\
G_{2,k} &= (-\overline{A}_k\omega^*_k) \left(-\frac{1-b}{bU}\phi_{4(j-1)-2,k} - \frac{1-b}{bU}\ R_W\phi_{4(j-1),k} + \frac{1}{bU}\phi_{4j-2,k} + \frac{R_L}{bU}\ \phi_{4j,k} \right),\\
G_{3,k} &= \overline{A}_k \left(\phi_{4j-2,k} - \phi_{4(j-1)-2,k} \right),\\
G_{4,k} &= (-\overline{A}_k\omega^*_k) \left(\phi_{4(j-1)-2,k} + R_W\ \phi_{4(j-1),k} \right),\\
G_{5,k} &= \overline{A}_k \left(\phi_{4j-1,k} - \phi_{4(j-1)-1,k} \right), && (4.56)\\
G_{6,k} &= \overline{A}_k\ \phi_{4(j-1),k},\\
G_{7,k} &= (-\overline{A}_k\omega^*_k) \left(\phi_{4(j-1)-2,k} + R_W\ \phi_{4(j-1),k} \right),
\end{aligned}
$$

$$G_{8,k} = \overline{A}_k \, \phi_{4j,k},$$

$$G_{9,k} = (-\overline{A}_k \omega_k^*) \, (\phi_{4j-2,k} + R_L \, \phi_{4j,k}) - (1-b) G_{7,k}.$$

These integrations have been derived similarly to those for the windward conductor but higher order terms are needed due to a more complex form of the aerodynamic forces acting on the leeward conductor.

4.2.7 Stability of limit cycles

Constants $\overline{A}_i$ and $\overline{\Psi}_j$ and frequencies ω_i^*, $i = 1, 2, \ldots, N_p$, $j = 1, 2, \ldots, m$, are found by letting $\dot{\overline{A}}_i(t) = \dot{\overline{\Psi}}_j = 0$ in equations (4.29) and (4.30) and solving the resulting nonlinear algebraic equations. Therefore the approximation of a limit cycle, given by equation (2.4), can be determined.

The stability of a limit cycle is determined by the $(N_p + m) * (N_p + m)$ characteristic matrix, $[S_c]$, constructed from equation (2.24) of Chapter 2. The signs of the real parts of the eigenvalues of $[S_c]$ determine the stability of the limit cycle. When $m \neq 0$, one eigenvalue is always zero because all the ψ_i are measured with respect to a reference mode. If all other eigenvalues have negative real parts, the limit cycle is stable.

4.2.8 Time integration

A direct time integration of the equations of motion is performed separately in the principal coordinate system (4.27) as an alternative approach. The algorithm is summarized by equations (2.25) to (2.28).

4.3 Results and discussion

An oscillator idealization of a fixed windward conductor model is employed to validate the computer program by duplicating data for an existing example of wake-induced oscillations of a leeward conductor. Two bare conductors are represented as circular cylinders; the leeward cylinder is supported by linear springs and dampers. The rotation of each cylinder is neglected due to its symmetrical cross-section. Aerodynamic force coefficients are identical to those used in references [5] and [7] so that the results can be checked directly with those given in reference [7]. Agreement between the present limit cycle amplitudes and those presented in reference [7] is within 6% for both time-averaged and numerically integrated solutions although different numerical schemes are employed.

The second oscillator example used to verify the program involved two moving cylinders; both the windward and leeward cylinders are mounted on linear springs and dampers as in reference [6]. The coupling springs and dampers between the cylinders simulate the effects of spacers. The solutions from the two methods agree reasonably (less than 10% difference in the limit cycle amplitudes) for the final limit cycle oscillation loci of both cylinders. Moreover, the difference in the limiting motions between the current approach and that considering a time delay caused by retardation of the wake flow traveling from the windward to the leeward conductor has also been checked. However, only the numerical time integration is performed in this instance. Figure E.1 shows the limit cycles obtained by the two approaches. The limit cycle amplitudes have approximately the same order for the example used in reference [6]. Therefore, the time delay is neglected in the current approach when determining the trend of the galloping and wake-induced motions.

A finite element model employing two conductors, one located in the wake of the other, is a more realistic simulation of a full scale transmission line. It has been

found that about 20 percent more ice is formed on the windward than the leeward conductor and the ice shape on the leeward conductor tends to be more roundish [75]. However, a typical D–shaped ice conductor and a bare cylinder are used as the windward and leeward conductors to simulate probably an extreme icing situation. The two conductors having fixed ends are separated greatly (0.45 m), compared to the conductors' diameter of 18.82 mm, so that the aerodynamic forces on the conductors are similar to those on two individual single conductors. Information on the single D–shaped conductor can be found in reference [1] when the wind's angle of attack on the D-section is 40^o. On the other hand, $C_L = 0$, $C_D = 1.2$ and $C_\theta = 0$ for a bare cylinder [6]. Other parameters used in the calculation are: wind speed = 4.1 m/s, $\rho_{air} = 1.2929\ kg/m^3$, conductors' length = 125.88 m and a pretension = 21733 N. A total of twenty, 3-node cable elements (ten for each conductor) is used. Node numbers are from 1 to 41 and from 2 to 42 on the windward and leeward conductors, respectively.

Interphase spacers are used to control galloping at least to the extent of preventing phase to phase contacts. The spacers are normally located away from the towers, sometimes at or near mid–span, sometimes at the one–third or one–quarter points of the span [76]. The number of spacers used in the separate calculations is increased progressively from 1 to 2, 3, 4, 9 and, finally, to 19. For example, one spacer is located in the initial calculation at the mid–span; then two rigid spacers are used to connect nodes 13 and 14 and nodes 27 and 28, respectively, at approximately the one–third span, and so on.

The three lowest frequency modes having close frequency values are used to compute the limit cycle of the conductors. Their mode shapes are shown in Figure 4.3. They correspond to one loop, symmetrical modes when one spacer is located at the mid–span. The horizontal motion, vertical movement and the rotation dominate

the first, second and third modes, respectively. Due to the three closely spaced natural frequencies, a 1 : 1 : 1 resonant case is considered when the KB averaging method is employed. The limit cycles at the mid-spans of the windward and leeward conductors are shown in Figure 4.4 to be similar. Compared to the conductors' motions computed at mid–span when a different number of spacers are used, it can be seen that the limiting motions for the cases involving one, two or three spacers are very similar. Consequently, slightly increasing the number of spacers hardly affects the limit cycle's amplitude, but should lead eventually to the bulk motion described in Chapter 3. Therefore, interphase spacers do not prevent galloping but they force the motions into a mode in which a flashover is much less likely [76].

4.4 Concluding Remarks

A nonlinear finite element model of galloping and wake–induced oscillations has been developed for a twin–bundle, electrical transmission line when the conductors are coupled by spacers and coated with ice. Three node, isoparametric cable elements are used to account for the conductors' geometrical nonlinearity as well as their prestress and the nonlinear aerodynamic loads. On the other hand, two node beam elements represent the relatively rigid spacers. The aerodynamic forces are obtained from static measurements in a wind tunnel by assuming a quasi-steady behavior. The initiation of galloping is investigated numerically by using a conventional stability analysis. Limit cycle amplitudes, if periodic or quasi–periodic oscillations occur, are obtained from an efficient, Krylov-Bogoliubov time averaging method. However, a computationally expedient, time marching algorithm is used to compute the response for those instances where the averaging procedure cannot be employed. A stability analysis is also performed for all motions.

The Krylov-Bogoliubov method of time averaging as well as a numerical integration scheme are employed separately to solve the nonlinear equations of motion for wake-induced oscillations. The two solutions agree well for the limit cycles. The time averaging method is an efficient way of solving the nonlinear equations for wake–induced flutter with a fixed windward conductor. When the windward conductor is allowed to move, however, the nonlinear equations become more complicated and the convergence of the iterations used to solve the equations becomes slower. Therefore, the initial guess for the limit cycles becomes more important in reducing the computational effort.

Iced twin conductors tend to move as a bundle when they are coupled by rigid spacers. Sub-span motions are caused by the differences in the aerodynamic forces as well as the properties of the two conductors. Examples are given to illustrate typical oscillations of both bare and iced, twin conductors.

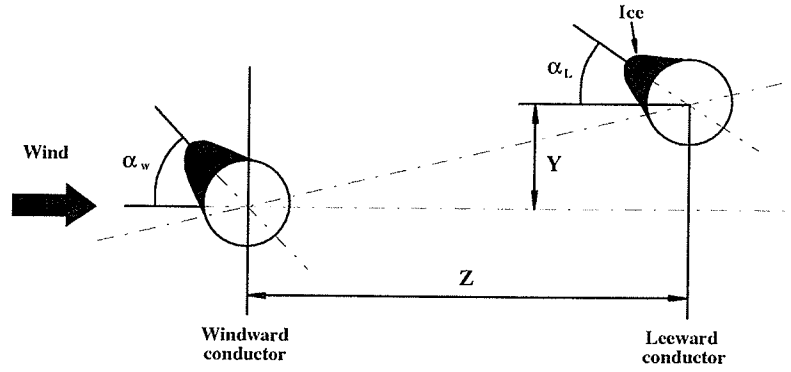

(a)

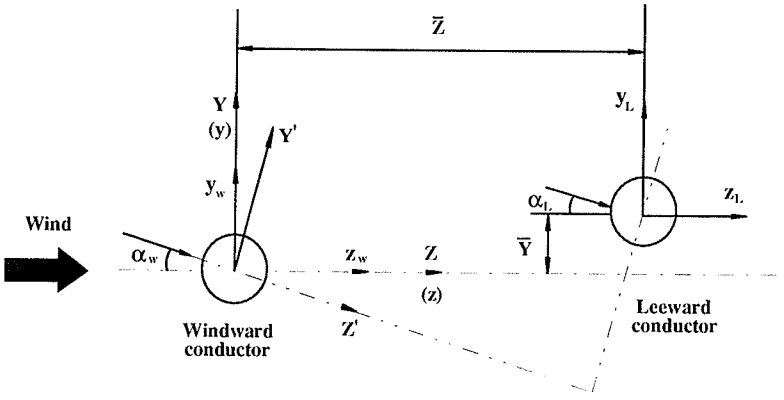

(b)

Figure 4.1: (a) Location and orientation of conductors in aerodynamic wind tunnel tests and (b) coordinate system defining the relative positions between the windward and leeward conductors

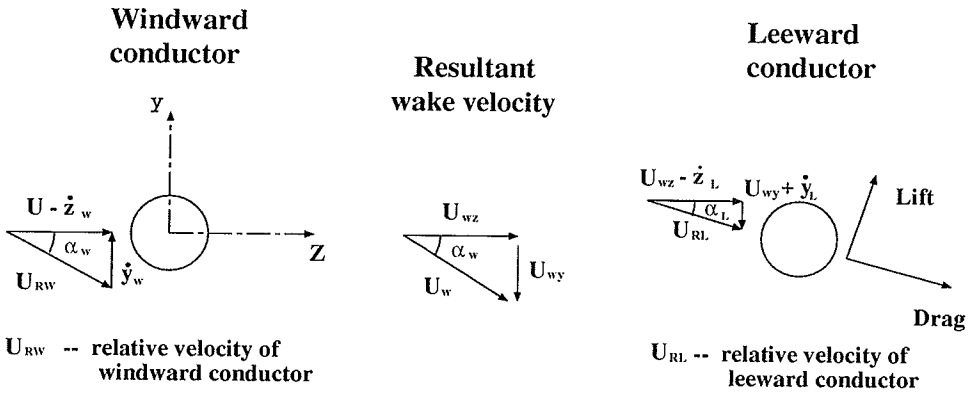

Figure 4.2: Relative movement of the windward and leeward conductors

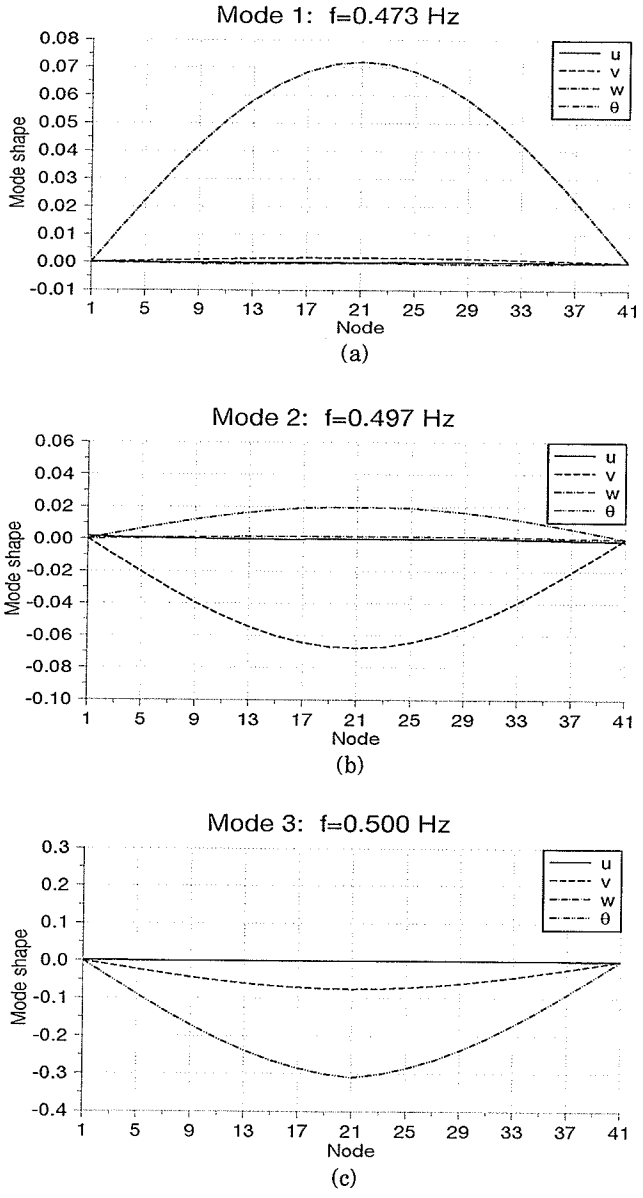

Figure 4.3: Lowest three frequency, single loop, symmetrical mode shapes of each conductor in a twin bundle having one spacer

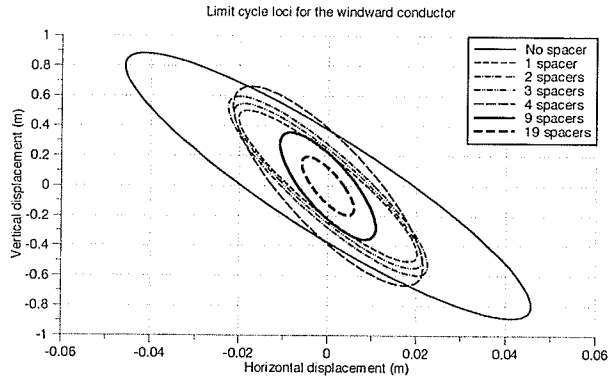

(a)

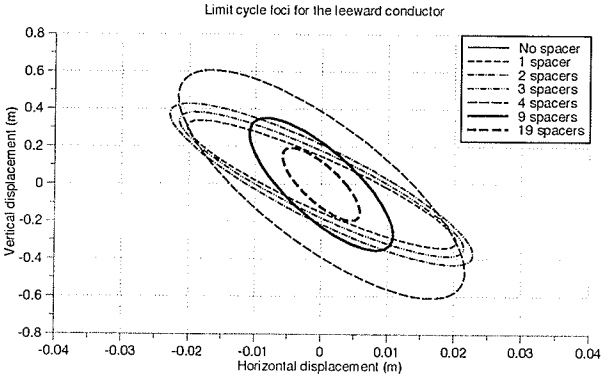

(b)

Figure 4.4: Mid–span limit cycle loci obtained from KB method by using the lowest three frequency modes for the (a) windward and (b) leeward conductors

Chapter 5

Conclusions and Future Work

Two nonlinear finite element models of galloping and wake–induced oscillations have been developed for an iced twin–bundle, electrical transmission line. Systematic procedures are formulated to investigate the initiation of galloping and to compute the limit cycles when galloping happens.

The initiation of galloping is investigated numerically by using a conventional stability analysis for both models. Limit cycle amplitudes, if periodic or quasi–periodic oscillations occur, are obtained from an efficient, Krylov-Bogoliubov (KB) time averaging method. However, a computationally expedient, time marching algorithm is also developed to compute the response for those instances where the averaging procedure cannot be employed. A stability analysis is also performed for all motions.

Iced twin conductors tend to move as a bundle when they are coupled by rigid spacers. Sub-span motions are caused by the differences in the aerodynamic forces as well as the properties of the two conductors. Calculating the bulk motion of a transmission line is much more computationally efficient by employing an equivalent single conductor model. when the full span motions are of sole interest. Therefore, this simpler model can be used for a quick check in a preliminary design of a new transmission line.

Recommended future work is suggested next.

1. A detailed parametric investigation can be undertaken expeditiously to evaluate

the influence of a particular parameter on either the initiation of galloping or on the limiting amplitudes. Design curves in the form of the stability boundaries can also be constructed.

2. The effects of an auxiliary control device can be incorporated in both finite element models. Then the number and locations of the devices can be optimized to help alleviate galloping.

3. The number of conductors in a bundle can be extended to three or four in both models. However, the DOF may become very large for the wake–induced model. Then the efficiency of the equivalent single conductor model becomes more obvious.

Bibliography

[1] Manitoba Hydro, "Modelling of Conductor Galloping : Vol I & II", Canadian Electrical Association Report, Project No. 321 T 672, Montreal, Canada (1992).

[2] Manitoba Hydro, "Modelling of Conductor Galloping : Phase II", Canadian Electrical Association Report, Project No. 321 T 672A, Montreal, Canada (1995).

[3] Nakamura, Y., "Galloping of bundled power line conductors", Journal of Sound and Vibration, 73(3), 363 – 377 (1980).

[4] Bokaian, A., "Galloping of a circular cylinder in the wake of another", Journal of Sound and Vibration, 128(1), 71 – 85 (1989).

[5] Price, S.J. and Piperni, P., "An investigation of the effect of mechanical damping to alleviate wake–induced flutter of overhead power conductor", Journal of Fluids and Structures, 2, 53 – 71 (1988).

[6] Price, S.J. and Abdallah, R., "On the efficacy of mechanical damping and frequency detuning in alleviating wake–induced flutter of overhead power conductors", Journal of Fluids and Structures, 4(1), 1 – 34 (1990).

[7] Price, S.J. and Maciel, Y., "Solution of the nonlinear equations for wake–induced flutter via the Krylov and Bogoliubov method of averaging", Journal of Fluids and Structures, 4, 519 – 540 (1990).

[8] Desai, Y.M., Popplewell, N., Shah, A.H. and Chan, J.K., "Static and dynamic behavior of mechanical components associated with electrical transmission lines–III(A)", The Shock and Vibration Digest, 21(12), 3 – 8 (1989).

[9] Johns, D.J., "Wind excited behavior of structures VI", The Shock and Vibration Digest, 22(4), 3 – 16 (1992).

[10] Nakamura, Y.,"Recent research into bluff-body flutter", Journal of Wind Engineering and Industrial Aerodynamics, 23(1-2), 1 – 10 (1990).

[11] Currie, I.G., Havard, D.G. and Pon, C.J.,"Literature survey on aeolian vibration excitation of bundled conductors", Final Report, Canadian Electrical Association, Project No. 177–T–510 (1987).

[12] Fijino, Y., Ito, M. and Yamaguchi, H., "Three-dimensional behavior of galloping in telecommunication cables", Journal of Wind Engineering and Industrial Aerodynamics, 30(1-3), 17 -26 (1988).

[13] Yamaguchi, H., "Analytical study on growth mechanism of rain vibration of cables", Journal od Wind Engineering and Industrial Aerodynamics, 33(1-2), 73 – 80 (1990).

[14] Stumpf, P., Popplewell, N., and Balakrishnan, S., "Procedure for automating wind tunnel measurements", *CANCAM 93: Proc of 14th Canadian Congress of Applied Mechanics*, Queen's Univ, Kingston, Ontario, Canada, Volume I, 321 – 322 (1993).

[15] Stumpf, P., Barrett, W., Popplewell, N, Shah, A.H. and Balakrishnan, S., "Automated wind tunnel measurements", *Experimental Techniques*, The Society for Experimental Mechanics, INC, 18(4), 34 – 38 (1994).

[16] Bouchard, G. and MacComber, P., "Numerical computation of the quasi–steady wind forces on a noncircular two–dimensional shape", *Symp on Flow–Induced Vibration and Noise–Volume 6*, ASME 1992, FED–Vol.138/PVP–Vol.245, 131 – 146 (1992).

[17] Parkinson, G., "Phenomena and modelling of flow–induced vibrations of bluff bodies", Prog. Aerospace Sci., 26, 169 – 224 (1989).

[18] Rawlins, C.B., "Galloping stability of a single conductor with electricity research laboratories' wet snow shape 2", Alcoa Conductor Products Company, Technical Note No. 29 (1991).

[19] Yu, P., Desai, Y.M. and Popplewell, N., "Predicting the galloping of an electrical transmission line", CANCAM 91: Proceedings of Thirteenth Canadian Congress of Applied Mechanics, University of Manitoba, Winnipeg, Manitoba, 522 – 523 (1991).

[20] Yu, P., Popplewell, N. and Shah, A.H., "A geometrical approach assessing instability trends for galloping", Journal of Applied Mechanics, ASME, 58(3), 784 – 791 (1991).

[21] Yu, P., Desai, Y.M., Popplewell, N., Shah, A.H., Harvard, D.G. and Chan, J.K., "Simple modelling of the galloping of electrical lines: an overview", Presented at the CEA Meeting, Toronto, Canada, May (1991).

[22] Yu, P., Shah, A.H. and Popplewell, N., "Inertially coupled galloping of iced conductors", Journal of Applied Mechanics, ASME, 59(1), 140 – 145 (1992).

[23] Desai, Y.M., Shah, A.H. and Popplewell, N., " Galloping analysis for two–degree–of–freedom oscillator", Journal of Engineering Mechanics, 116(12), 2583 – 2602 (1990).

[24] Jones, K.F., Coupled vertical and horizontal galloping, *J of Eng Mechanics*, 118(1), 92 – 107 (1992).

[25] Yu, P., Desai, Y.M., Shah, A.H., and Popplewell, N., Three–degree–of–freedom model for galloping. Part 1: formulation, *J of Eng Mech*, 119(12), 2404 – 2425 (1993).

[26] Yu, P., Desai, Y.M., Popplewell, N. and Shah, A.H., "Three–degree–of–freedom model for galloping. Part 2: solutions", *J of Eng Mech*, 119(12), 2426 – 2448 (1993).

[27] Desai, Y.M., "Modelling of planar transmission line galloping", Ph.D Thesis, Dept. of Civil Engineering, University of Manitoba (1991).

[28] Byun, G.S. and Egdert, R.I., "Two–degree–of–freedom analysis of power line galloping by describing function method", Electric Power System Research, 21(3), 187 – 193 (1991).

[29] Desai, Y.M., Shah, A.H., Popplewell, N. and Data, S.K., "Micro-based, iteractive software for the simple modelling of conductor galloping", Enginnering Software, Edited by Ramakrishnan, C.V., Varadarajan, A. and Desai, C.S., Narosa Publishing House, 491 – 495 (1989).

[30] Abdel-Rohman, M., "Galloping of tall flexible structures due to smooth flow", Proceedings of the Ninth International Conference on Offshore Mechanics and Arctic Engineering 1990. Volume I: Offshore Technology–Part B, Publ. by ASME, New York, USA, 313 – 320 (1990).

[31] Aboul-ella, F., "New Iterative analysis of cable-stayed structures", Computers and Structures, 40(3), 549 – 554 (1991).

[32] Pheinsusom, P. and Fujino, Y., "Effect of turbulence on the modal interaction in galloping of structure with two closely-spaced natural frequencies", Japan Society of Civil Engineers (Proc. of JSCE No.398/I–10), 193 – 196 (1988).

[33] Pheinsusom, P., Fujino, Y. and Ito, M., "Galloping of tower–like structure with two closely–spaced natural frequencies", Journal of Wind Engineering and Industrial Aerodynamics, 32(1-2), 189 – 198 (1989).

[34] Leipholz, H., "Direct variational methods and eigenvalue problems in engineering", Noordhoff International Publishing, Leyden, Netherlands (1977).

[35] Nayfeh, A. H., "Introduction to perturbation techniques", John Wiley and Sons, New York (1981).

[36] van Horssen, W.T.," An asymptotic theory for a class of initial – boundary value problems for weakly nonlinear wake equations with an application to a model of the galloping oscillations of overhead transmission lines", SIAM J. Appl. Marh., 48(6), 1227 – 1243 (1988).

[37] van Horssen, W.T., "Asymptotics for a system of nonlinearly coupled wave equations with an application to the galloping oscillations of overhead transmission lines", Quarterly of Applied Mathematics, 47(2), 197 – 219 (1989).

[38] Nataraj, C. and Nelson, H.D., "A collocation method for the investigation of periodic solutions in nonlinear systems", Diagnostic, Vehicle Dynamic, and Dpecial Topics: Presented at the 1989 ASME Design Technical Conferences, 12th Biennial Conference on Mechanical Vibration and Nise, Montreal, Quebec, Canada, Published by ASME, New York, NY, USA, DE v 18-5, 325 – 330 (1989).

[39] Simiu, E. and Cook, G.R., "Chaotic motions of self–excited forced and autonomous square prisms", Journal of Enginnering Mechanics, 117(2), 241 – 259 (1991).

[40] Simiu, E., Cook, G.R. and Alibe, B., "Aldebraic approximation of attractors for galloping oscillators", Journal of Sound and Vibration, 146(1), 170 – 175 (1991).

[41] Oliveria, A.R.E. and Mansour, W.M., "Nonlinear analysis of wake–induced oscillations", IEEE Transactions on Power Apparatus and Systems, PAS–104(3), 727 – 732 (1985).

[42] Abdallah, R. and Price, S.J., "Wake–induced flutter of power transmission lines: effect of mechanical damping", CANCAM 89: Proceedings of Twelfth Canadian Congress of Applied Mechanics, Carleton University, Ottawa, 674 – 675 (1989).

[43] Zan, S.J., Wardlaw, R.L., and Stumpf, P., "Wind tunnel tests of an iced bundled–conductor madel", *CANCAM 93: Proc of 14th Canadian Congress of Applied Mechanics*, Queen's Univ, Kingston, Ontario, Canada, Volume I, 249 – 250 (1993).

[44] Valerio, N.R. and Price, S.J., "A nonlinear stability analysis of a single flexible cylinder in an array of rigid cylinders", CANCAM 89: Proceedings of Twelfth Canadian Congress of Applied Mechanics, Carleton University, Ottawa, 674 – 675 (1989).

[45] Paidoussis, M.P. and Price, S.J., "The mechanisms underlying flow-induced instabilities of cylinder arrays in crossflow", Journal of Fluid Mechanics, 187, 45 – 59 (1988).

[46] Marn, J. and Catton, I., "On stabilty analysis of a flexible cylinder in an array of rigid cylinders", Journal of Fluid Engineering, 114, 12 – 19 (1992).

[47] Corless, R.M. and Parkinson, G.V., "A mathematical model of the combined effects of vortex–induced vibration and galloping", Journal of Fluids and Structures, 2(3), 203 – 220 (1988).

[48] Corless, R.M. and Parkinson, G.V., "Mathematical modelling of the combined effects of vortex–induced vibration and galloping –Part II", *Symp. on Flow–Induced Vibration and Noise –Vol 6*, ASME 1992, FED–Vol. 138/PVP–Vol. 245, 39 – 62(1992).

[49] Diana, G., Cheli,F., Manenti, A., Nicolini, P. and Tavano, F., "Oscillation of bundle conductors in overhead lines due to turbulent wind", *IEEE Transactions on Power Delivery*, 5(4), 1910 – 1919 (1991).

[50] Tsui, Y.T., "On wake–induced vibration of a conductor in the wake of another via a 3-D finite element method", Journal of Sound and Vibration, 107(1), 39 – 58 (1986).

[51] Liao, M., Popplewell, N. and Shah, A.H., "Low–frequency oscillations of a twin–bundle", *Proc of Third Int Congress on Air–and Structure–Borne Sound and Vib*, Montreal, Canada, Volume 2, 763 – 770 (1994).

[52] Liao, M., Popplewell, N. and Shah, A.H., "Galloping of twin–bundled conductors", *Eng Mechanics Symp:Proc of the 1994 CSCE Annual Conf*, Winnipeg, Manitoba, Volume IV, Mechanics, 13 – 18 (1994).

[53] Yu, P., Popplewell, N. and Shah, A.H., "Instability trends of inertially coupled galloping, part I: initiation", *Journal of Sound and Vib*, 183(4), 663 – 678 (1995).

[54] Yu, P., Popplewell, N. and Shah, A.H. , "Instability trends of inertially coupled galloping, part II: periodic vibrations", *Journal of Sound and Vib*, 183(4), 679 – 691 (1995).

[55] Havard, D.G. and Pon, C.J., "Use of detuning pendulums for control of galloping of single conductor and two and four conductor transmission lines", *Transactions of the 5th Intl. Workshop on the Atmospheric Icing of Structures*, Tokyo, Japan (1990).

[56] Pon, C.J., "Control of distribution line galloping", Ontario Hydro Research Division, Canadian Electrical Association Report No. 196–D–367, Toronto, Canada (1988).

[57] Pon, C.J. and Havard, D.G., "Field trials of galloping control devices for bundle conductor lines", Canadian Electrical Association Interim Report No. 133–T–386, Toronto, Canada (1990).

[58] Pon, C.J. and Havard, D.G., "Field testing of four conductor bundle spacer-dampers", *Paper presented at the Canadian Electrical Association 1991 Spring Meeting*, Engineering and Operation Division, Transmission Section, Toronto, Canada (1991).

[59] Richardson, A.S., "A study of galloping conductors on a 230kv transmission line", *Electric Power System Research*, 21(1), 43 – 55 (1991).

[60] Langmacker, D., Stegemann, G. and Streubel, H., "Separators on high–voltage overhead lines prevent disturbances of the electric power transmission", *Proc of the Int Conf on Large High Voltage Electrical Systems, CIGRE: Proc. 40th Session*, 22–08, Paris, France (1986).

[61] Havard, D.G., Pon, C.J. and Pohlman, J.C., "Reduction of tower head dimensions through galloping controls", *Proc of the 3rd Int Workshop on the Atmospheric Icing of Structures*, Vancouver, Canada, 441 – 449 (1986).

[62] Havard, D.G., "Galloping conductor control–status 1988", 4th Int. Conf. on Atmospheric Icing of Structures, Paris, France, Sept. (1988).

[63] Welt, F. and Modi, V.J., "On the control of instabilities in field–structure interactions problems", *Proc of the Conf on Control of Distributed Parameter Systems 1986*, Los Angeles, U.S.A., 115 – 120 (1986).

[64] Bogoliubov, N. N. and Mitropolsky, Y. A., "Asymptotic methods in the theory of non–linear oscillations", Hindustan Publishing Corpn. (INDIA), Delhi (1961).

[65] Gilchrist, A. O., "The free oscillations of conservative quasilinear systems with two degrees of freedom", *Int. J. Mech. Science*, 3, 286 – 311 (1961).

[66] Sethna, P. R., "Transients in certain autonomous multiple–degree–of–freedom nonlinear vibrating systems",*J. Appl. Mech.*, ASME, 85(Series E), 44 – 50 (1963).

[67] Desai, Y.M., Popplewell, N., Shah, A.H. and Buragohain, D.N., "Geometric nonlinear static analysis of cable supported structures", Comput. Struct., 29(6), 1001 – 1009 (1988).

[68] Zienkiewicz, O.C., "The finite element method", Third edition, McGraw–Hill, New York (1977).

[69] Gawronski, K.E., "Nonlinear galloping of bundle–conductor transmission lines", Ph.D Thesis, Clakson College of Technology (1977).

[70] Blevins, R. D., *Flow – induced vibration* (2nd edition). Van Nostrand Reinhold Co., New York (1990).

[71] Chadha, J., "A study of the mechanisms of conductor galloping and its control." Ontario Hydro Research Division Report No. 74 – 212 – K (1974).

[72] Richardson, A. S., Jr., "Dynamic analysis of lightly iced conductor galloping in two degrees of freedom." *Proc. IEE*, 128 (Pt. C)(4), 211 – 218 (1981).

[73] Nigol, O. and Buchan, P. G., "Conductor galloping : Torsional mechanism – Parts I and II." *Tr. IEEE*, PAS – 96 (2), 699 – 720 (1981).

[74] Gortemaker, P. C. M., "Galloping conductors and evaluation of the effectiveness of inspan dampers." *Kema Science and Technical Reports (Netherlands)*, 2(4), 27 – 39 (1984).

[75] Stumpf, P., "Determination of Aerodynamic Forces for Iced Single and Twin–Bundled Conductors", M. Sc. Thesis, University of Manitoba, Winnipeg, Canada (1994).

[76] Transmission Line Reference Book, *Wind – Induced Conductor Motion: EPRI*, Palo Alto, California (1979).

[77] Tsui, Y.T. and Tsui, C.C., "On wake–induced flutter of a circular conductor in the wake of another", Journal of Pressure Vessel Technology, 102(), 125 – 137 (1980).

[78] Stumpf, P. and Ng, H.C.M., "Investigation of aerodynamic stability for selected inclined cables and conductor cables", B. Sc. Thesis, University of Manitoba, Winnipeg, Canada (1990).

[79] Nath, B., *Fundamentals of finite elements for engineers.*The Athlone Press of the University of London (1974).

[80] Bathe, K.J., "Finite element procedures in engineering analysis", Prentice–Hall, Inc., New Jersay (1982).

[81] Desai, Y.M., Yu, P., Shah, A.H. and Popplewell, N.,*Journal of Sound and Vibration*, 190(1), (in press) (1996).

[82] Simpson, A. and Flower, J.W., "An improved mathematical model for the aerodynamic forces on tandem cylinders in motion with aeroelastic applications", *Journal of Sound and Vibration*, 51(2), 183 – 217 (1977).

[83] McConnell, K.G. and Chang, C.N., "A study of the axial–torsional coupling effect on a sagged transmission line", *Experimental Mechanics*, 324 – 329 (1986)

[84] Veletsos, A.S. and Darbre, G.R., "Dynamic stiffness of parabolic cables", *International Journal of Earthquake Engineering and Structural Dynamics*, 11, 367 – 401 (1983).

[85] Mathur, R.K., Shah, A.H., Trainor, P.G.S. and Popplewell, N., "Dynamics of a guyed transmission tower system", *Transactions of IEEE: Power Delivery*, PWRD – 2 (3), 908 – 916 (1987).

[86] Clough, R.W. and Penzien, J., *Dynamics of structures*. New York: McGraw–Hill (1975).

Appendix A

Elements

A.1 Cable element

Each three–node isoparametric element idealizing a conductor is referred to the fixed global X, Y, Z axes and the initial intrinsic coordinate, S, which is along the cable's center [67], as shown in Figure A.1(a). By denoting the displacements in the X, Y and Z directions to be U, V and W, respectively, and the rotation about S to be θ, the element nodal displacement vector, $\{q^e\}$, is defined as

$$\{q^e\} =< \{q_1\}\ \{q_2\}\ \{q_3\} >^T \tag{A.1}$$

where

$$\{q_k\} =< U_k\ V_k\ W_k\ \theta_k >^T, \quad k\ =\ 1,2,3. \tag{A.2}$$

The global coordinates and the displacements of a reference cross section's axis of rotation are represented, respectively, by

$$< X\ Y\ Z >^T = \sum_{k=1}^{3} N_k\ < X_k\ Y_k\ Z_k >^T \tag{A.3}$$

and

$$< U\ V\ W\ \theta >^T\ =\ [N]\{q^e\} \tag{A.4}$$

where the parabolic shape functions, N_k, are given by

$$\begin{aligned} N_1 &= \frac{2S^2}{L_e^2} - \frac{3S}{L_e} + 1 \\ N_2 &= -\frac{4S^2}{L_e^2} + \frac{4S}{L_e} \end{aligned} \tag{A.5}$$

and

$$N_3 = \frac{2S^2}{L_e^2} - \frac{S}{L_e}.$$

Here L_e is the length of the element. Moreover, the shape function matrix, $[N]$, is

$$[N] = [\ N_1[I_4]\ \ N_2[I_4]\ \ N_3[I_4]\ ] \tag{A.6}$$

where $[I_4]$ is the 4×4 identity matrix.

Mass matrix

The consistent element mass matrix takes the standard integral form

$$[M^e] = \int_0^{L_e} [N]^T[\mu][N]dS, \tag{A.7}$$

where

$$[\mu] = \int_{A_T} \rho[R]^T[R]dA.$$

The $\rho(y, z)$ is the mass density of a conductor per unit volume over the total cross sectional area, A_T, of an iced-conductor's profile in the local y-z plane coordinates. Furthermore, the 3×4 matrix $[R]$ is defined by

$$[R] = \begin{bmatrix} 1 & 0 & 0 & 0 \\ 0 & 1 & 0 & -z \\ 0 & 0 & 1 & y \end{bmatrix}.$$

Stiffness matrix

The element stiffness matrix, $[{K_T}^e]$, is decomposed into the three components given by

$$[K^e] = [K_E^e] + [{K_\sigma}^e] + [K^e]_{ice}, \tag{A.8}$$

where $[K_E^e]$, $[{K_\sigma}^e]$ and $[K^e]_{ice}$ are the large deformation elastic and initial stress (or geometric) stiffness matrices as well as the stiffness matrix due to the eccentric ice

weight. The later is linearized in the vicinity of the static profile [1]. Details of the computation of $[K_E^e]$, $[K_\sigma{}^e]$ and $[K^e]_{ice}$ are given in reference [81].

A.2 Beam element

Spacers are simulated by using two node, beam elements whose mass matrix is established by lumping equal parts of the element's total mass to the nodal points. The beam element's standard stiffness matrix is formulated by employing local coordinates and four DOF at each nodal point [79]. (See Figure A.1(b).) By transforming the local nodal displacement vector into global coordinates and denoting the displacements in the X, Y, Z directions and the angular rotation to be U, V, W, and θ, respectively, the element nodal displacement vector, $\{q^e\}$, is

$$\{q^e\} =< \{q_1\}\ \{q_2\} >^T . \tag{A.9}$$

Here $\{q_k\} = < U_k\ V_k\ W_k\ \theta_k >^T$, $k = 1,\ 2$, refers to the nodal displacement vectors on the windward and leeward conductors, respectively. Angle θ is the same as the rotation of a conductor about its center because it is assumed that the spacers and conductors are attached rigidly.

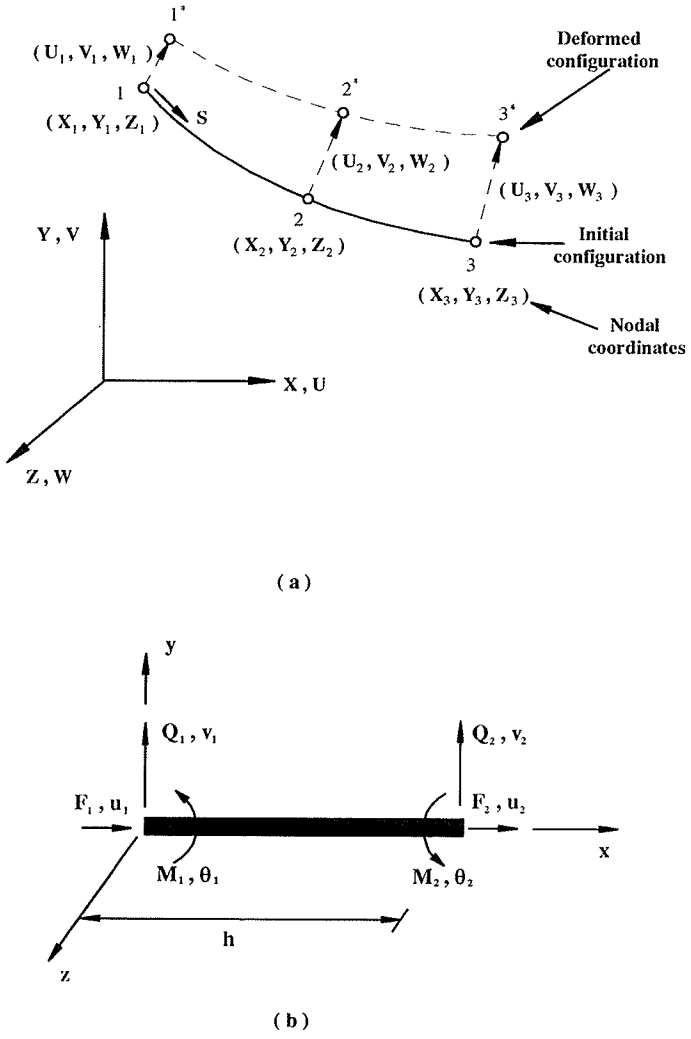

Figure A.1: (a) Three–node cable element and (b) two–node beam element

Appendix B

Element Structural Matrices

B.1 Elements of $[M^e]$

The symmetric mass matrix $[M^e]$ is given by

$$[M^e] = \frac{L_e}{2940}\begin{bmatrix} [M_1] & [M_2] & [M_3] \\ [M_2] & [M_4] & [M_5] \\ [M_3] & [M_5] & [M_6] \end{bmatrix} \tag{B.1}$$

where the non-zero elements of the symmetric matrices $[M_i], i = 1, 2, \ldots, 6$ are

$$\begin{aligned} m_{i1,1} &= m_{i2,2} = m_{i3,3} = \sum_{p=1}^{3} P_p^i \mu_p \quad ; \quad m_{i2,4} = \sum_{p=1}^{3} P_p^i S_{y_p} \\ m_{i3,4} &= \sum_{p=1}^{3} P_p^i S_{zp} \quad ; \quad m_{i4,4} = \sum_{p=1}^{3} P_p^i I_{\theta p} \quad . \end{aligned} \tag{B.2}$$

Here, μ_p, S_{y_p}, S_{zp} and $I_{\theta p}$ are the per unit length mass, first mass moment of area about the y and z axis and the mass moment of area about the S axis, respectively, at the pth node of the iced conductor. Constants P_1^i, P_2^i and P_3^i are listed in Table B.1.

B.2 Elements of $[K_E^e]$, $[K^e]_{ice}$ and $[K_\sigma^e]$

The upper triangular terms of the symmetric matrix $[K_E^e]$ are given next for a bare cable element having constant axial rigidity, AE, an axial-torsional coupling parameter, B_1, whose significance has been outlined in [83], and torsional rigidity,

GJ, over its length L_e. (Refer to [1, 27] for details.)

$$\frac{15L_e^{\,3}}{AE}k^e_{El,n} = P_4(\Delta\zeta_1^i)^2 + P_5(\Delta\zeta_2^i)^2 + P_6\Delta\zeta_1^i\Delta\zeta_2^i \quad , \quad i=1,2,3 \tag{B.3}$$

$$\frac{15L_e^{\,3}}{AE}k^e_{El,n} = P_7\Delta\zeta_1^1\Delta\zeta_1^2 + P_8(\Delta\zeta_1^1\Delta\zeta_2^2 + \Delta\zeta_2^1\Delta\zeta_1^2) + P_9\Delta\zeta_2^1\Delta\zeta_2^2 \qquad i=1,2\ ;\ j=2,3 \text{ and } i\neq j \tag{B.4}$$

$$\frac{3L_e^{\,2}}{B_1}k^e_{El,n} = P_{10}\zeta_1^i + P_{11}\zeta_2^i + P_{12}\zeta_3^i \quad , \quad i=1,2,3 \tag{B.5}$$

$$k^e_{El,n} = \frac{GJ}{3L_e}P^i_{13} - \frac{gL_e}{2940}\sum_{p=1}^{3}P^i_pS_{zp} \quad , \quad i=1,2,\ldots,6 \tag{B.6}$$

$$\begin{aligned}
k^e_{E3,i+4} &= k^e_{Ei,7} \quad , \quad i=1,2\\
k^e_{E3,i+8} &= k^e_{Ei,11} \quad , \quad i=1,2\\
k^e_{E7,i+8} &= k^e_{Ei+4,11} \quad , \quad i=1,2\\
k^e_{E2,1+4i} &= k^e_{E1,2+4i} \quad , \quad i=1,2\\
k^e_{E4,(i+4p)} &= k^e_{Ei,4(p+1)} \quad , \quad p=1,2 \quad , \quad i=1,2,3\\
k^e_{E8,i+8} &= k^e_{Ei+4,12} \quad , \quad p=1,2 \quad , \quad i=1,2,3\\
k^e_{E6,9} &= k^e_{E5,10}
\end{aligned} \tag{B.7}$$

Constants P_i and $P^i_j, j=1,2,3,13\ , i=4,\ldots,12$ are presented in Table B.1 along with l, n and i (where applicable). The g in equation (B.6) is the gravitational constant and the first mass moment of area at the element's kth node, S_{zk}, is

$$S_{zk} = \int_{A_T} \rho\ y\ dA \quad . \tag{B.8}$$

Stiffness terms, which involve S_{zk} in equation (B.6), are computed by first linearizing the restoring moment as $gS_z\sin\theta \approx gS_z\theta$ at the typical iced cross section shown in Figure 4.2(b); and then forming the equivalent element terms from

$$[K^e]_{ice} = -g\int_0^{L_e}[N]^T\begin{bmatrix}0&0&0\\0&0&0\\0&0&S_z\end{bmatrix}[N]\ dS \tag{B.9}$$

where

$$S_z = \sum_{k=1}^{3} N_k \, S_{zk} \quad . \tag{B.10}$$

The undefined quantities in equations (B.3) through (B.5) are

$$\Delta\zeta_j^i \;=\; \zeta_{j+1}^i \;-\; \zeta_j^i \quad , \quad i = 1,2, \quad j = 1,2$$

and

$$[\zeta_k^1 \quad \zeta_k^2 \quad \zeta_k^3]^T \;=\; [X_k^* \quad Y_k^* \quad Z_k^*]^T \tag{B.11}$$

where

$$[X_k^* \quad Y_k^* \quad Z_k^*]^T \;=\; [X \quad Y \quad Z]^T \;+\; [U \quad V \quad W]^T \tag{B.12}$$

are the deformed coordinates of the kth node of the element.

The symmetric, geometric stiffness matrix $[K_\sigma^e]$, on the other hand, is approximated as

$$[K_\sigma^e] \approx \frac{T_1}{3L_e}[K_{\sigma 1}^e] \;+\; \frac{(T_2 \;-\; T_1)}{6L_e}[K_{\sigma 2}^e] \tag{B.13}$$

where

$$[K_{\sigma i}^e] \;=\; \begin{bmatrix} (7 - \delta_2^i 4\sqrt{3})[\bar{I}] & (-8 + \delta_2^i 4\sqrt{3})[\bar{I}] & [\bar{I}] \\ (-8 + \delta_2^i 4\sqrt{3})[\bar{I}] & 16[\bar{I}] & (-8 - \delta_2^i 4\sqrt{3})[\bar{I}] \\ [\bar{I}] & (-8 - \delta_2^i 4\sqrt{3})[\bar{I}] & (7 + \delta_2^i 4\sqrt{3})[\bar{I}] \end{bmatrix} \quad , \; i = 1,2 \tag{B.14}$$

$$[\bar{I}] \;=\; \text{diag}[1 \;\; 1 \;\; 1 \;\; 0] \tag{B.15}$$

and T_1 and T_2 indicate the static tension at Gauss points 1 and 2 which are located distance $S = L_e(\sqrt{3} - 1)/2\sqrt{3}$ and $S = L_e(\sqrt{3} + 1)/2\sqrt{3}$ from node 1, respectively. Furthermore, $\delta_2^1 = 0$ and $\delta_2^2 = 1$.

B.3 Elements of $[C_U{}^e]$ and $[K_U{}^e]$

The non – zero elements of matrices $[C_U{}^e]$ and $[K_U{}^e]$ of equation (2.16) are given below.

(a) Elements on the windward conductor

$$\begin{aligned}
c^{e}_{u4i-2,4i-2} &= P^i_{14}\ P^i_{15}\ {}^ia_{y1} \\
c^{e}_{u4i-1,4i-2} &= P^i_{14}\ P^i_{15}\ {}^ia_{z1} \\
c^{e}_{u4i,4i-2} &= P^i_{14}\ d_i\ P^i_{15}\ {}^ia_{\theta 1} \\
c^{e}_{u4(i-1)+j,4i} &= R_i\ c^{e}_{u4(i-1)+j,4i-2} \quad ; \quad j=2,3\ ;\ i=1,2,3 \qquad \text{(B.16)} \\
k^{e}_{u4i-2,4i} &= P^i_{14}\ P^i_{16}\ {}^ia_{y1} \\
k^{e}_{u4i-1,4i} &= P^i_{14}\ P^i_{16}\ {}^ia_{z1} \\
k^{e}_{u4i,4i} &= P^i_{14}\ d_i\ P^i_{16}\ {}^ia_{\theta 1} \quad ; \quad i=1,2,3\ . \qquad \text{(B.17)}
\end{aligned}$$

Here i represents the ith node of a cable element and constants P^i_{14}, R_i, ${}^ia_{y1}$ etc correspond to the ith node. Moreover,

$$\begin{aligned}
P^1_{14} &= P^3_{14} = \frac{1}{2}P^2_{14} = \frac{L_e}{4} \\
P^i_{15} &= \frac{P^i_{16}}{U_{zi}} = \frac{1}{2}\rho_{air}\ U_{zi}\ d_i \quad , \quad i=1,2,3. \qquad \text{(B.18)}
\end{aligned}$$

(b) Elements on the leeward conductor

$$\begin{aligned}
c^{eL}_{u4i-2,4i-2} &= -\ P^i_{14}\ P^i_{15}\ {}^iB_{0,5/b} \\
c^{eL}_{u4i-1,4i-2} &= -\ P^i_{14}\ P^i_{15}\ {}^iC_{0,5}/b \\
c^{eL}_{u4i,4i-2} &= -\ P^i_{14}\ d_i\ P^i_{15}\ {}^iD_{0,5}/b \\
c^{eL}_{u4(i-1)+j,4i} &= R_{Li}\ c^{e}_{u4(i-1)+j,4i-2} \quad ; \quad j=2,3,4\ ;\ i=1,2,3 \qquad \text{(B.19)} \\
k^{eL}_{u4i-2,4i} &= P^i_{14}\ P^i_{16}\ {}^iB_{0,5}
\end{aligned}$$

$$
\begin{aligned}
k^{eL}_{u4i-1,4i} &= P^i_{14}\ P^i_{16}\ {}^iC_{0,5} \\
k^{eL}_{u4i,4i} &= P^i_{14}\ d_i\ P^i_{16}\ {}^iD_{0,5} \\
k^{eL}_{u4i-2,4i-1} &= P^i_{14}\ P^i_{16}\ {}^iB_{0,2} \\
k^{eL}_{u4i-1,4i-1} &= P^i_{14}\ P^i_{16}\ {}^iC_{0,2} \\
k^{eL}_{u4i,4i-1} &= P^i_{14}\ d_i\ P^i_{16}\ {}^iD_{0,2} \\
k^{eL}_{u4i-2,4i-2} &= P^i_{14}\ P^i_{16}\ {}^iB_{1,1} \\
k^{eL}_{u4i-1,4i-2} &= P^i_{14}\ P^i_{16}\ {}^iC_{1,1} \\
k^{eL}_{u4i,4i-2} &= P^i_{14}\ d_i\ P^i_{16}\ {}^iD_{1,1} \quad ; \quad i = 1,2,3\ .
\end{aligned}
\tag{B.20}
$$

$$
\begin{aligned}
c^{eW}_{u4i-2,4i-2} &= -\ P^i_{14}\ P^i_{15}\ {}^iB' \\
c^{eW}_{u4i-1,4i-2} &= -\ P^i_{14}\ P^i_{15}\ {}^iC' \\
c^{eW}_{u4i,4i-2} &= -\ P^i_{14}\ d_i\ P^i_{15}\ {}^iD' \\
c^{eW}_{u4(i-1)+j,4i} &= R_{Wi}\ c^{e}_{u4(i-1)+j,4i-2} \quad ; \quad j = 2,3,4\ ;\ i = 1,2,3 \\
k^{eW}_{u4i-2,4i} &= P^i_{14}\ P^i_{16}\ {}^iB_{0,3} \\
k^{eW}_{u4i-1,4i} &= P^i_{14}\ P^i_{16}\ {}^iC_{0,3} \\
k^{eW}_{u4i,4i} &= P^i_{14}\ d_i\ P^i_{16}\ {}^iD_{0,3} \\
k^{eW}_{u4i-2,4i-1} &= -\ P^i_{14}\ P^i_{16}\ {}^iB_{0,2} \\
k^{eW}_{u4i-1,4i-1} &= -\ P^i_{14}\ P^i_{16}\ {}^iC_{0,2} \\
k^{eW}_{u4i,4i-1} &= -\ P^i_{14}\ d_i\ P^i_{16}\ {}^iD_{0,2} \\
k^{eW}_{u4i-2,4i-2} &= -\ P^i_{14}\ P^i_{16}\ {}^iB_{1,1} \\
k^{eW}_{u4i-1,4i-2} &= -\ P^i_{14}\ P^i_{16}\ {}^iC_{1,1} \\
k^{eW}_{u4i,4i-2} &= -\ P^i_{14}\ d_i\ P^i_{16}\ {}^iD_{1,1} \quad ; \quad i = 1,2,3\ ,
\end{aligned}
\tag{B.21, B.22}
$$

where

$$\begin{aligned} {}^iB' &= -{}^iB_{1,1}z_0 + {}^iB_{0,2}y_0 + {}^iB_{0,3} - \frac{1-b}{b}{}^iB_{0,5} \\ {}^iC' &= -{}^iC_{1,1}z_0 + {}^iC_{0,2}y_0 + {}^iC_{0,3} - \frac{1-b}{b}{}^iC_{0,5} \\ {}^iD' &= -{}^iD_{1,1}z_0 + {}^iD_{0,2}y_0 + {}^iD_{0,3} - \frac{1-b}{b}{}^iD_{0,5}. \end{aligned} \tag{B.23}$$

The superscripts L and W refer to the leeward and windward conductor, respectively. Equation (2.16) may be modified to

$$\{F_L{}^e\} = [C_U{}^{eL}]\{\dot{q}^e\} + [K_U{}^{eL}]\{q^e\} + [C_U{}^{eW}]\{\dot{q}^{eW}\} + [K_U{}^{eW}]\{q^{eW}\} \quad , \tag{B.24}$$

where $\{q^e\}$ is the element nodal displacement vector and $\{q^{eW}\}$ is the vector of nodal displacements of the corresponding element on the windward conductor.

B.4 Beam elements of $[K^e]$

The symmetric stiffness matrix for a 4-DOF beam element is given by [79]

$$[K^e] = \frac{E}{h^3}\begin{bmatrix} ah^2 & 0 & 0 & 0 & -ah^2 & 0 & 0 & 0 \\ 0 & 12I & 0 & 6Ih & 0 & -12I & 0 & 6Ih \\ 0 & 0 & 12I & 0 & 0 & 0 & -12I & 0 \\ 0 & 6Ih & 0 & 4Ih^2 & 0 & -6Ih & 0 & 2Ih^2 \\ -ah^2 & 0 & 0 & 0 & ah^2 & 0 & 0 & 0 \\ 0 & -12I & 0 & -6Ih & 0 & 12I & 0 & -6Ih \\ 0 & 0 & -12I & 0 & 0 & 0 & 12I & 0 \\ 0 & 6Ih & 0 & 2Ih^2 & 0 & -6Ih & 0 & 4Ih^2 \end{bmatrix} \tag{B.25}$$

where E, I, h and a are Young's modulus, the second moment of area, length of the element and the cross–sectional area, respectively.

Table B.1: Expressions for P_k^i and P_k.

i	1	2	3	4	5	6
P_1^i	273	140	-21	112	-56	-21
P_2^i	140	112	-56	1344	112	140
P_3^i	-21	-56	-21	112	140	273
l	i	i	i	$i+4$	$i+4$	$i+8$
n	i	$i+4$	$i+8$	$i+4$	$i+8$	$i+8$
P_4	183	-216	33	272	-56	23
P_5	23	-56	33	272	-216	183
P_6	-66	112	-46	-224	112	-66
l	i	i	i	$i+4$	$i+4$	$i+8$
n	j	$j+4$	$j+8$	$j+4$	$j+8$	$j+8$
P_7	183	-216	33	272	-56	23
P_8	-33	56	-23	-112	56	-33
P_9	23	-56	33	272	-216	183
l	i	i	i	$i+4$	$i+4$	$i+8$
n	4	8	12	8	12	12
P_{10}	-15	16	-1	-16	0	1
P_{11}	16	-16	0	0	16	-16
P_{12}	-1	0	1	16	-16	15
i	1	2	3	4	5	6
l	4	4	4	8	8	12
n	4	8	12	8	12	12
P_{13}^i	7	-8	1	16	-8	7

Appendix C

Expressions for K_{ST}, K_{I_x} and K_{I_z}

Remote spans are modelled as linear static springs, K_{ST}, in the X direction as shown in Figure 1.1. The support insulator string, which is considered to be a single, vertical rigid bar, pin connected to the tower's arm, is also modelled as a linear static spring that has components K_{Ix} and K_{Iz} in the X and Z directions, respectively. The K_{ST} and K_{Ix} affect the diagonal stiffness term associated with the corresponding U displacement whereas K_{Iz} contributes to the analogous term associated with the W displacement. It can be shown that [1, 84, 85]

$$\begin{aligned} \frac{1}{K_{ST}} &= \frac{L}{AE} + \frac{{p_y}^2 {L_x}^3}{12H^3} \\ K_{Ix} &= \frac{1}{L_I}\left(p_y L + \frac{W_I}{2}\right) \end{aligned} \tag{C.1}$$

and

$$K_{Iz} = K_{Ix} + \frac{2H}{L_x} \tag{C.2}$$

where L_x and L are the horizontal span length and total length of the iced cable between adjacent towers, respectively. Moreover, p_y is the total vertical load, $H(= T\frac{\partial S}{\partial X})$ is the horizontal component of the static tension whilst L_I and W_I are the length and weight of an insulator string, respectively.

Appendix D

Computation of the Damping Matrix, $[C]$

Elements $c_{i,j}$ of the symmetric, structural damping matrix $[C]$ are approximated by assuming mass and stiffness proportional Rayleigh damping [86]. Hence

$$c_{i,j} = \beta_{k1} m_{i,j} + \beta_{k2} k_{i,j} \quad , i \geq j \tag{D.1}$$

where the symbolic subscript k takes the value y when $i \neq 3n, n = 1, 2, 3, \ldots, 3 \times n_p$, and θ when $i = 3n$. Furthermore, $m_{i,j}$ and $k_{i,j}$ are elements of the structural mass and stiffness matrices, respectively. The β_{k1} and β_{k2} in equation (D.1) are computed from

$$\begin{aligned} \beta_{k1} &= \frac{2\xi_{k1}\omega_{k1}\omega_{k2}}{(\omega_{k1} + \omega_{k2})} \\ \beta_{k2} &= \frac{2(\xi_{k2}\omega_{k2} - \xi_{k1}\omega_{k1})}{({\omega_{k2}}^2 - {\omega_{k1}}^2)} \end{aligned} \tag{D.2}$$

where ξ_{k1} and ξ_{k2} are the measured damping ratios for two k modes having the respective natural frequencies ω_{k1} and ω_{k2}. If ξ_{k2} are not measured, β_{k2} are considered to be zero in equation (D.1) and β_{k1} is simply

$$\beta_{k1} = 2\xi_{k1}\omega_{k1} \quad . \tag{D.3}$$

Appendix E

Formulation Considering Flow Retardation

The aerodynamic forces on the leeward conductor are determined by the air flow or the resultant wake around it. The magnitude and direction of the resultant wake velocity, in turn, depend on the free stream speed, relative separation between the two conductors and motion of the windward conductor. Therefore, there is a coupling between the windward conductor's motion and the aerodynamic forces on the leeward conductor, as indicated in Chapter 4. However, it takes a finite time for a flow traveling from the windward to arrive at the leeward conductor. Thus, what influences the leeward conductor at time t originated from the windward conductor at time $t-\tau$, where τ is the time delay. The effects of τ on the leeward conductor will be considered here [6, 82]. The derivation of the forces follow the same procedure described in Chapter 4 except that the variables involving the windward conductor from equations (4.16) to (4.25) will be those at time $t-\tau$ instead of at time t.

The aerodynamic forces in equation (4.21) become

$$\begin{aligned} F_y &\doteq \frac{1}{2}\rho_{air}U_e^2 dC_y(\alpha_{W\tau}, \alpha_L, y, z), \\ F_z &\doteq \frac{1}{2}\rho_{air}U_e^2 dC_z(\alpha_{W\tau}, \alpha_L, y, z), \\ \text{and} & \\ M_\theta &\doteq \frac{1}{2}\rho_{air}U_e^2 d^2 C_\theta(\alpha_{W\tau}, \alpha_L, y, z), \end{aligned} \tag{E.1}$$

where

$$U_e^2 = U^2 \left\{ \left[1 + \frac{(1-b)\dot{Z}_{W\tau} - \dot{Z}_L}{bU} \right]^2 + \left[\frac{(1-b)\dot{Y}_{W\tau} - \dot{Y}_L}{bU} \right]^2 \right\}.$$

The subscript τ indicates the retarded variable at time $t-\tau$ and C_i, $i = y, a, \theta$, has the same expression as in equation (4.22) after changing α_W into $\alpha_{W\tau}$. The variables used in the last equation are defined as

$$\begin{aligned} y &= Y' - y_0 \\ z &= Z' - z_0, \\ \alpha_{W\tau} &= \theta_{W\tau} - tan^{-1}\left(\frac{\dot{Y}_{W\tau}}{U - \dot{Z}_{W\tau}}\right), \\ \alpha_L &= \theta_L - \tan^{-1}(U_{LY}/U_{LZ}), \end{aligned} \tag{E.2}$$

where

$$U_{LY} = b\ \dot{Y}_{W\tau} - \dot{Y}_{W\tau} + \dot{Y}_L$$

and

$$U_{LZ} = b\ (U - \dot{Z}_{W\tau}) + \dot{Z}_{W\tau} - \dot{Z}_L. \tag{E.3}$$

Other variables, which are shown in Figure E.2, can be found as follows.

$$\begin{aligned} Y' &= \left(\frac{Y_B - Y_{W\tau} + Y_L}{cos\alpha_{W\tau}} - \frac{\mu d}{Ub}\dot{Y}_L \right) exp\left(\frac{1-b_m}{b_m}\ \frac{\dot{Z}_{W\tau}}{U} \right), \\ Z' &= \left(\frac{\overline{Z}\ -\ Y\ sin\alpha_{W\tau}}{cos\alpha_{W\tau}} \right) + \frac{\mu d}{Ub}\dot{Z}_L, \\ \overline{Z} &= \tau\ (U - \dot{Z}_{W\tau}) \\ \tau &= (\ Z_B\ -\ Z_{W\tau}\ +\ Z_L\ )\ /\ U, \\ Z_{w\tau} &= \frac{Z_W - (Z_B + Z_L)\dot{Z}_W/U + \frac{1}{2}(Z_B/U)^2(1 + 2Z_L/Z_B)\ddot{Z}_W}{1 - \dot{Z}_W/U + Z_B\ddot{Z}_W/U^2}. \end{aligned} \tag{E.4}$$

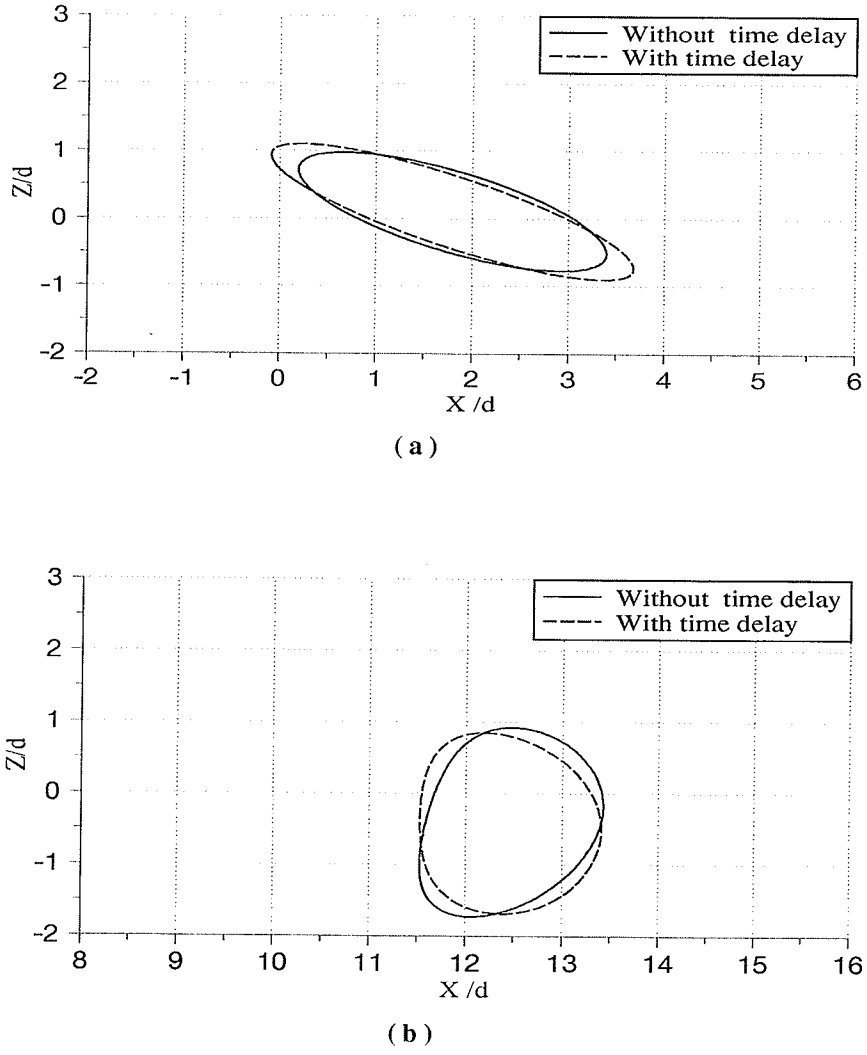

Figure E.1: Limit cycle loci for the (a) windward and (b) leeward conductor

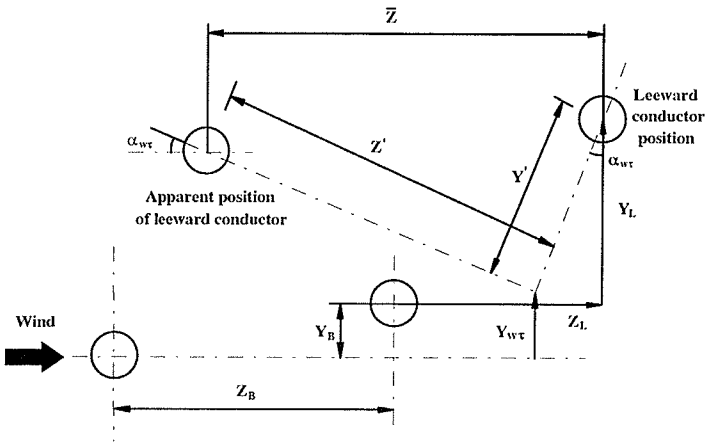

Figure E.2: Positions of the windward and leeward conductors